


SCIENTIFIC REPORTS



OPEN

The first Neanderthal remains from an open-air Middle Palaeolithic site in the Levant

Ella Been^{1,2}, Erella Hovers^{3,4}, Ravid Ekshtain³, Ariel Malinski-Buller⁵, Nuha Agha⁶, Alon Barash⁷, Daniella E. Bar-Yosef Mayer^{8,9}, Stefano Benazzi^{10,11}, Jean-Jacques Hublin¹¹, Lihl Levin², Noam Greenbaum¹², Netta Mitki³, Gregorio Oxilia^{13,10}, Naomi Porat ¹⁴, Joel Roskin^{15,16}, Michalle Soudack^{17,18}, Reuven Yeshurun¹⁹, Ruth Shahack-Gross¹⁵, Nadav Nir³, Mareike C. Stahlschmidt²⁰, Yoel Rak² & Omry Barzilai⁶

The late Middle Palaeolithic (MP) settlement patterns in the Levant included the repeated use of caves and open landscape sites. The fossil record shows that two types of hominins occupied the region during this period—Neandertals and *Homo sapiens*. Until recently, diagnostic fossil remains were found only at cave sites. Because the two populations in this region left similar material cultural remains, it was impossible to attribute any open-air site to either species. In this study, we present newly discovered fossil remains from intact archaeological layers of the open-air site 'Ein Qashish, in northern Israel. The hominin remains represent three individuals: EQH1, a nondiagnostic skull fragment; EQH2, an upper right third molar (RM³); and EQH3, lower limb bones of a young Neanderthal male. EQH2 and EQH3 constitute the first diagnostic anatomical remains of Neandertals at an open-air site in the Levant. The optically stimulated luminescence ages suggest that Neandertals repeatedly visited 'Ein Qashish between 70 and 60 ka. The discovery of Neandertals at open-air sites during the late MP reinforces the view that Neandertals were a resilient population in the Levant shortly before Upper Palaeolithic *Homo sapiens* populated the region.

The Middle Palaeolithic (MP) of the southern Levant is a significant period for the study of human evolution because two types of hominins, Neandertals and *Homo sapiens*, occupied the region at that time (see, for example, refs 1 and 2). Diagnostic fossil remains of the two species have been found in the Mediterranean woodland region, but until recently, they were discovered only at cave sites (Fig. 1). The absolute chronology of the Levantine MP fossils indicates that *H. sapiens* existed there between 120 and 90 ka and again from 55 ka on; Neandertals existed in that region between ca. 80 and ca. 55 ka^{3–16}. The genomic evidence suggests gene flow from early *H. sapiens* to

¹Department of Physical Therapy, Faculty of Health Professions, Ono Academic College, Kiryat Ono, 55107, Israel.

²Department of Anatomy and Anthropology, Sackler Faculty of Medicine, Tel Aviv University, Tel Aviv, 69978, Israel.

³Institute of Archaeology, the Hebrew University of Jerusalem, Jerusalem, 91905, Israel. ⁴Institute of Human Origins,

Arizona State University, P.O. Box 874101, Tempe, AZ, 85287-4101, Israel. ⁵MONREPOS Archaeological Research

Centre and Museum for Human Behavioural Evolution, Schloss Monrepos, D - 56567, Neuwied, Germany. ⁶Israel

Antiquities Authority, P.O. Box 586, Jerusalem, 91004, Israel. ⁷Faculty of Medicine in the Galilee, Bar Ilan University,

Zefat, 13115, Israel. ⁸Steinhardt Museum of Natural History, Tel Aviv University, Tel Aviv, 69978, Israel. ⁹Peabody

Museum of Archaeology and Ethnology, Harvard University, 11 Divinity Avenue, Cambridge, MA, 02138, USA.

¹⁰Department of Cultural Heritage, University of Bologna, Via degli Ariani 1, 48121, Ravenna, Italy. ¹¹Department of

Human Evolution, Max Planck Institute for Evolutionary Anthropology, Deutscher Platz 6, 04103, Leipzig, Germany.

¹²Department of Geography & Environmental Studies, University of Haifa, Haifa, 3498838, Israel. ¹³Department

of Biology, University of Florence, Via del Proconsolo, 12, 50122, Firenze, Italy. ¹⁴Luminescence Dating Lab,

Geological Survey of Israel, Jerusalem, 95501, Israel. ¹⁵Department of Maritime Civilizations, University of Haifa,

Haifa, 3498838, Israel. ¹⁶School of Sciences, Achva Academic College, Shikmim Mobile Post 79800, Shikmim, Israel.

¹⁷Department of Diagnostic Imaging, Chaim Sheba Medical Center, Tel Hashomer, 52621, Israel. ¹⁸Sackler Faculty

of Medicine, Tel Aviv University, Tel Aviv, 69978, Israel. ¹⁹Zinman Institute of Archaeology, University of Haifa, Haifa,

3498838, Israel. ²⁰School of Archaeology, University College Dublin, Belfield, Dublin 4, Ireland. Correspondence and

requests for materials should be addressed to E.B. (email: beenella1@gmail.com)

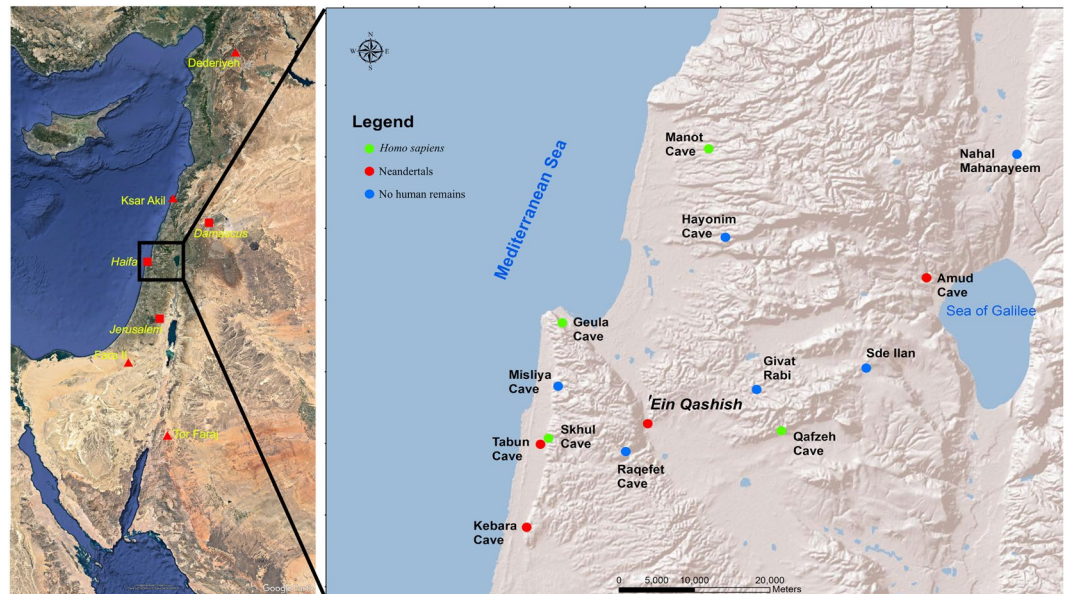


Figure 1. Left: Major Middle Palaeolithic sites (triangles) and modern cities (squares) in the Near East. Right: Location of 'Ein Qashish and other Middle Palaeolithic sites in northern Israel. The map was generated using ESRI ArcInfo v10.4.

the eastern Altai Neandertals ca. 100 ka¹⁷ and flow from Neandertals to *H. sapiens* between ca. 60 and 50 ka¹⁸. In the Levant, the archaeological record cannot distinguish between these two MP populations. The lithic variability observed in the Levantine MP is not clearly taxonomy related (ref. 19 for a different view see ref. 20). The two populations left similar material culture remains—in particular, lithic industries that include the Levallois technology. In addition, the populations seem to have had similar settlement and mobility patterns in respect to the use of caves for habitation and burials; at Tabun, these populations used the same cave diachronically^{12, 13, 21, 22}.

The discovery of several previously unknown MP open-air sites in the Mediterranean woodland region in the last decade diverted much of the research focus to MP behaviors associated with the open landscape (e.g., ref. 23). In the absence of taxonomically informative fossil remains, it was impossible to attribute these (as well as previously reported) open-air sites to either Neandertals or *H. sapiens*. Therefore, it was also difficult to determine these species' settlement patterns and territorial behavior within the Levant. The new discovery of Neandertal remains at the late MP open-air site of 'Ein Qashish provides a window into the settlement and mobility pattern of the Neandertals of northern Israel.

The Site

'Ein Qashish is located on the south bank of the Qishon stream in the Jezreel Valley, facing the eastern slopes of Mount Carmel, Israel (Fig. 1). Excavations at the site in 2009–2011 exposed remains of a Late Mousterian occupation on the Qishon floodplain^{24–28}.

In 2013, the site was subjected to an extensive salvage excavation during which an area of ca. 650 m² was dug to a maximum depth of 4.5 m (ref. 29; SI 1). The stratigraphy consists of six sedimentary layers comprising four occupational horizons (Fig. 2). The 2013 excavation is laterally and stratigraphically contiguous to the original excavation, with a similar depositional context. The sediments are composed mainly of black heavy clays representing the flood plain of the palaeo-Qishon stream and coarse cobbles transported by short, steep, fast-flowing streams off the eastern flanks of Mount Carmel (refs 25 and 26; SI 1). The site sequence was dated through optically stimulated luminescence (OSL), which puts the time range of all the examined archaeological horizons at ca. 70–60 ka (SI 2 Table 1), similar to the range of dates of the stratigraphic sequence of the 2009–2011 excavation, established through the same dating techniques²⁶.

The Context of the Hominin Remains. The hominin remains from 'Ein Qashish represent three individuals that were found in three distinct layers (Fig. 2).

Specimen EQH1 is a nondiagnostic skull fragment that was discovered in a mechanically dug geological trench prior to the 2013 excavation (ref. 29; SI 1). The stratigraphic position of the fossil corresponds to Layer 1, the lowest in the documented sections in the site's vicinity. Layer 1 is absent from the sequence in the archaeological excavation itself (N. Greenbaum, pers. obs.). Contextual data for the layer are poor.

The second fossil, EQH2, is an upper third molar (Fig. 3) from Layer 5a, in Area A. The fossil was found associated with flint artefacts and faunal remains in a horizon with refitted lithic items (51 refitted items in 21 aggregates) (SI 1), indicating a moderately disturbed *in situ* context.

The best-preserved specimen is EQH3, consisting of five lower limb bones—a femur, two tibiae, and two fibulae (Fig. 4)—associated with an occupational horizon in stratigraphic Layer 3b, Area B (for details of the archaeological context, see SI 1). The femur and the left tibia of EQH3 were found articulated. The bones were aligned along the same axis, with the right tibia parallel to the left (Fig. 4A,B). One of the two fibulae (B1880)

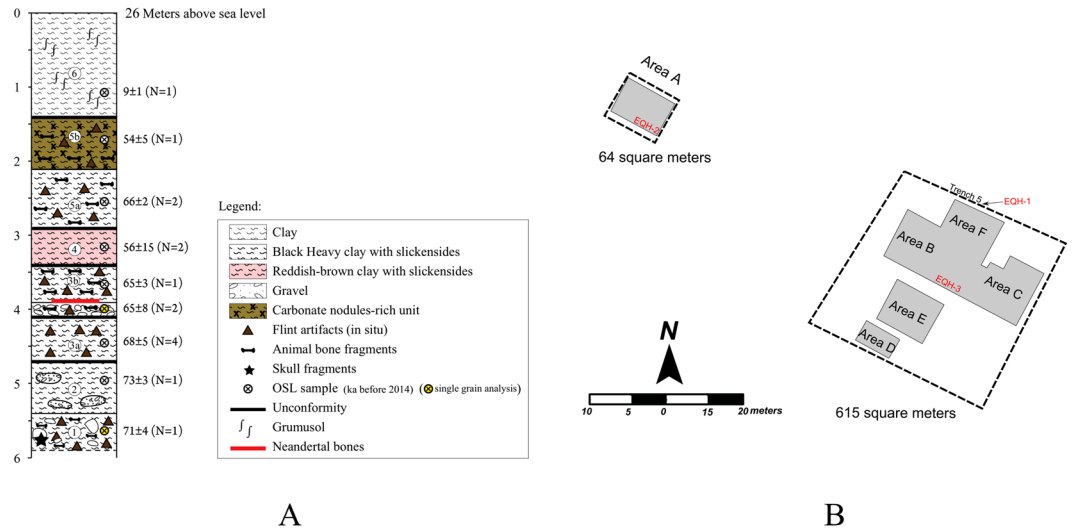


Figure 2. Schematic plan of 'Ein Qashish. (A) Compiled stratigraphic section with vertical locations of OSL dates, in thousands of years, and hominin fossils. (B) Plan of excavation areas with spatial locations of hominin fossils.

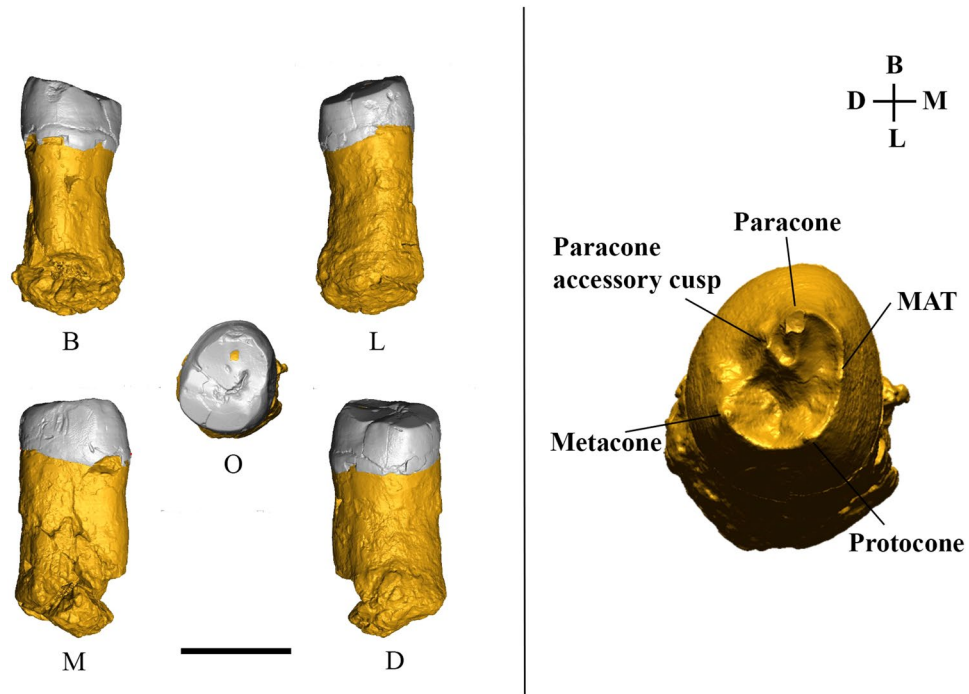


Figure 3. 3D digital model of specimen EQH2, an upper right third molar. Left: Various views—B, buccal; L, lingual; M, mesial; D, distal; O, occlusal. The black bar represents 1 cm. Right: The enamel-dentine junction (EDJ) surface of EQH2.

was discovered ca. 50 cm north of the femur-tibia cluster, and the other fibula (B12255), ca. 70 cm south of the cluster (Fig. 4A). Finds other than human remains in this particular horizon comprise fresh flint artefacts (with 21 refitted items from four aggregates); fragmented animal bones; limestone clasts, including potential manuports (possibly anvils); ochre; a roe deer antler and a seashell, *Hexaplex trunculus* (Linnaeus, 1758) (SI 1). OSL dating of sediments directly above and below EQH3 puts the fossil at 65 ± 8 ka (SI 2).

EQH2. EQH2 is an upper right third molar (RM³) on which both the crown (with a mesiodistal [MD] length of 8.3 mm and buccolingual [BL] length of 9.7 mm) and the root (with a length of 14.3 mm) are preserved. The moderate wear of the tooth, with the dentine exposed on the paracone cusp, corresponds to wear stage (category) 3 of Molnar’s dental attrition classification³⁰. In an occlusal view, the crown outline is oval, and although tooth

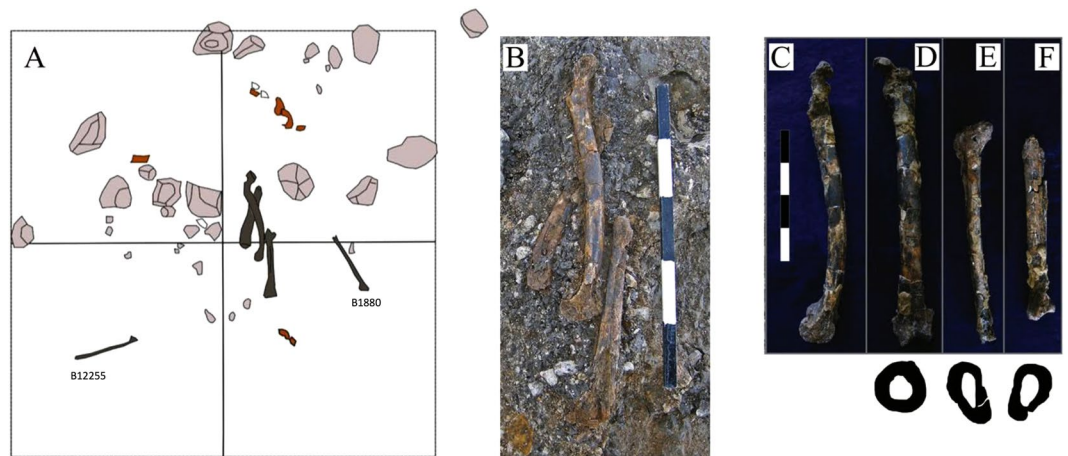


Figure 4. Specimen EQH3. (A) The spatial location of the five lower limb bones of EQH3 (dark brown); specimens B1880 and B12255 are fibulae. Pink: stones; reddish-brown: faunal remains. (B) The bones *in situ*. Note the partial articulation of the left femur and left tibia. (C) Left femur, medial view. (D) Left femur, anterior view; midshaft cross section (underneath). (E) Left tibia, anterior view; midshaft cross section (underneath). (F) Right tibia, anterior view; midshaft cross section (underneath).

wear has removed most of the occlusal features, three main cusps (the protocone, paracone, and metacone) can be identified (Fig. 3, right). At the enamel-dentine junction (EDJ) (Fig. 3, right; SI 3 Table 1), two accessory cusps (the mesial accessory tubercle [MAT] and paracone accessory cusp) are present, but there is no trace of the distolingual cusp (the hypocone) or Carabelli's cusp. An interproximal wear facet (length, 3.81 mm; width, 4.19 mm) is visible only on the mesial side of the tooth (Fig. 3, left). The tooth is hypertaurodontic and does not show root bifurcation.

We compared the MD and BL crown diameters of EQH2 to the diameters in tooth samples from Neandertals, early *H. sapiens*, Upper Palaeolithic *H. sapiens*, and recent *H. sapiens* (SI 3 Table 2; SI 3 Fig. 1). There is a large overlap in the distribution of the MD and BL diameters in our comparative sample. The values obtained for EQH2 are the lowest among the fossils and are closest to the values obtained for the Neandertal specimens Saccopastore 1, Amud 1, and Tabun 1 and the Upper Palaeolithic *H. sapiens* specimen Kostenki XIV (SI 3 Fig. 1). With regard to the relative enamel thickness (RET) index, the z score computed for the EQH2 RET value (18.9) is closer to the Neandertal mean than to the means of early, Upper Palaeolithic, and recent *H. sapiens* (SI 3 Tables 3, 4). Dental tissue volumes and root measurements of EQH2 and the comparative sample (SI 3 Fig. 2; SI 3 Tables 4, 5) show that the root of EQH2 is somewhat larger than in the comparative sample. The computed z score for EQH2's root length, total root volume, pulp volume, and root pulp volume is closer to that of the Neandertals, whereas the coronal pulp volume is closer to that of Upper Palaeolithic *H. sapiens* and the cervical plane area is closer to that of recent *H. sapiens*.

The cross-validation linear discriminant analysis of four root variables (root length, root volume, pulp volume, and cervical plane area) shows that 23 modern humans (92% of our sample) and all Neandertals in our sample were correctly classified and attributes EQH2 to *H. neanderthalensis* with a P_{post} of 70%. Note that if we remove the cervical plane area from the analysis, EQH2 is attributed to *H. neanderthalensis* with a P_{post} value of 81%.

EQH3. The lower limb bones of EQH3 consist of a left femur, two tibiae, and two fibulae. Out of the five lower limb bones, only the femur and two tibiae are preserved enough for analysis (Fig. 4C–F). The femur is essentially complete (Fig. 4). The femoral shaft is highly curved on the sagittal plane (i.e., anteroposteriorly), with the apex of the curvature located distal to the midshaft. The midshaft shape ratio (with a pilastric index of 99.1) indicates a rounded cross section (the anteroposterior diameter and mediolateral diameter are nearly equal) (Fig. 4; SI 4 Table 3). The midshaft robusticity index (14.9) indicates a highly robust femur. The midshaft cross-sectional area is large, with a relatively high percentage of cortical bone. All of these features are well-documented Neandertal characteristics that differ considerably from the more gracile femur of early and recent *H. sapiens*. There, the midshaft has a drop-shaped cross section and is straight compared to that of the Neandertals^{31–36} (SI 4). The distal epiphysis of the EQH3 femur is relatively small, and the intercondylar fossa is extremely narrow, a feature that is not usually seen in either *H. sapiens* or Neandertals (SI 4).

The remains of the right tibia include the diaphysis distal to the soleal line and the distal epiphyses; the proximal part of the tibia is missing (Fig. 4). Nearly complete, the left tibia is missing only its medial malleolus. The tibial plateau is flat, with a robust intercondylar tubercle (the medial part of the intercondylar eminence).

Both tibiae exhibit fragmented and slightly distorted shafts, which are robust and narrow mediolaterally (platycnemic), similar to the tibia of Amud 1³⁷. The anterior crest of the right and left tibial shafts and the interosseous borders are smooth and rounded. At 81.5, the crural index indicates that the tibia is short relative to the femoral length. Again, most of the striking features of the tibiae are associated with Neandertal morphology: the robust shaft, the rounded anterior crest and interosseous border, and the low crural index. The morphology of these tibiae contrasts with that of the more gracile *H. sapiens* tibiae, which are characterized by generally angular anterior and interosseous crests and a high crural index^{38, 39}.

The lower limb bones of EQH3 were found close together, with some in articulation. All belong to a male Neandertal, and no duplicate bones were found, suggesting that these bones represent a single individual (SI 4). The estimated height of the individual is 163.6 cm, which is close to the mean height for male Neandertals (166.7 ± 5.9 cm) and significantly less than the considerable height of the *H. sapiens* specimens from Qafzeh and Skhul (185.1 ± 7.1 cm) (SI 4; ref. 40).

Computed tomography (CT) reveals the presence of the epiphyseal line at the distal end of the femur and the proximal and distal ends of the tibiae, indicating ossification stage three out of four^{41,42}. Thus, the individual's age at death can be estimated at 15–22 y (young adult) (SI 4).

The combination of a narrow intercondylar notch and a robust intercondylar tubercle is not often seen in the knee joints of hominins (SI 4). This unique morphology is associated with an avulsion fracture of the anterior cruciate ligament (ACL). Such a traumatic injury occurs most commonly in skeletally immature individuals, between the ages of 8 and 14 years⁴³. If this pathology was present in the knee of EQH3, the individual might have suffered from instability of the left knee joint and therefore would probably have attempted to minimize the weight borne by the left leg. The small articular surface of the distal femur might be the result of the pathology, given that articular surface area is directly related to the amount of axial pressure exerted on the joint (SI 4; ref. 44).

Discussion

The absolute dating of contexts associated with the Neandertal fossils from Tabun, Dederiyeh, Kebara, and Amud Caves suggests that Neandertals occupied the southern Levant between ca. 80 and ca. 55 ka^{3,6,10,12,13,45}. Because diagnostic hominin remains from open-air sites dated to this period were not available until now (e.g., refs 46 and 47), attributing the occupation of open-air sites to Neandertal settlement systems called for caution. However, the fossils EQH2 and EQH3 derive from two distinct stratigraphic horizons, and their associated OSL ages suggest that the open-air site of 'Ein Qashish was used repeatedly by Neandertals from 70 to 60 ka, a period contemporary with the occupation of the Kebara and Amud Caves.

The discovery of diagnostic Neandertal remains at the open-air site of 'Ein Qashish is unusual not only for the Levant but also for Europe, where only two sites, both of which are earlier, have yielded such diagnostic fossils: the French Tourville a Rivière and Biache Saint Vaast 2 sites, both dated to marine isotope stage 7^{48,49}.

The recovery of the two Neandertal fossils from 'Ein Qashish raises questions as to the nature of their depositional histories and the inhabitants' behavioral patterns. Whereas the tooth (EQH2) does not constitute a compelling indication of death at the site, the preservation of bones of two legs, as well as their partial articulation, suggests that the individual represented by EQH3 is likely to have died at the site or nearby. Given the bone state of preservation and articulation, the body remains must have been buried rather fast, either anthropogenically or naturally.

The presence of Neandertal fossil remains at MP sites can be interpreted as the result of intentional burial or non anthropogenic deposition (e.g., refs 50 and 56). To determine which of the scenarios applies to the 'Ein Qashish fossils, we evaluated several parameters that may distinguish between the two scenarios: articulation, flexed position, evidence of an excavated pit, intentional coverage of the bones, and the presence of grave goods. Given the available evidence, we cannot determine whether EQH3 is a burial or not. The partial articulation of the left femur and tibia, which attests to a flexed position of the knee (Fig. 4), may support a hypothesis of intentional burial. On the other hand, there are no other body parts of the individual, no visible indication of a pit or the intentional covering of a corpse, and no grave markers. A number of uncommon finds (a seashell, roe deer antler, and ochre) that were unearthed in the same archaeological horizon are not directly associated with the bones of EQH3.

The most informative aspect of the discovery of EQH3 is that it is a Neandertal. The stratigraphic association with a diverse set of material culture remains indicates a habitation context, and the stratigraphic sequence suggests that the locality was used repeatedly. The identification of EQH2 and EQH3 enables us, for the first time, to confidently attribute to Neandertals a set of assemblages from an open-air site in the southern Levant. This discovery in the flat topography of the palaeo-Qishon flood plain demonstrates that locomotor traits did not necessarily constrain Neandertals from exploiting landscapes other than the rugged mountainous terrain (contra⁵⁷; see also ref. 58) and, by extension, the ecological mosaic of topographically diverse environments.

Hypotheses regarding the demise of the Levantine Neandertals implicate competitive exclusion, direct competition^{1,59}, and the inability of the Neandertals to adapt to climate variability and deterioration (e.g., ref. 60). Recent studies focusing on various proxies from Kebara and Amud Caves show that climate change in the Mediterranean zone during the MIS 4 to early MIS 3 time span may not have been as drastic as suggested⁶¹ and that behavioral strategies enabled the Neandertals to cope with ecological change^{62,63}. Combined with the dates of the Kebara and Amud Neandertals, the repeated occupation of 'Ein Qashish in the open landscape during the Levantine late MP reinforces the view that despite possible early interbreeding events¹⁷, Neandertals constituted a resilient population in the Mediterranean ecological zone of the southern Levant shortly before the region was populated by Upper Palaeolithic *H. sapiens*^{12–14,16,21,64}.

Materials and Methods

EQH-2. High-resolution micro-CT images of EQH2 were obtained with a SkyScan1173 microtomographic system (at the Max Planck Institute for Evolutionary Anthropology, Leipzig, Germany) using the following scan parameters: 100 kV, 62 μ A, with an aluminum-copper filter (1.0 mm thick). Volume data were reconstructed using isometric voxels of 12.90 μ m. We segmented the image stack with a semiautomatic threshold-based approach in Avizo 8 (Visualization Sciences Group Inc.) to separate the enamel, the dentine, and the pulp chamber and to reconstruct a 3D digital model of the tooth (Fig. 3).

Before beginning the analysis, we oriented the tooth in Rapidform XOR2 software (INUS Technology, Inc., Seoul, Korea): using a spline curve, we manually digitized the cervical line and computed a best-fit plane (the

cervical plane; SI 3 Fig. 2) through the points of the curve. The tooth was then rotated until the cervical plane was parallel to the xy -plane of the Cartesian coordinate system. The mesiodistal (MD) and buccolingual (BL) crown diameters of EQH2 were measured directly on the digital model and compared with those of Neandertals, early *H. sapiens*, Upper Palaeolithic *H. sapiens*, and recent *H. sapiens* (SI 3 Table 2; SI 3 Fig. 1).

Enamel thickness and dental tissue data were analyzed according to guidelines set by Benazzi *et al.*⁶⁵. We measured the enamel volume (in mm^3), dentine volume (in mm^3 , including the volume of the crown pulp chamber), and enamel-dentine junction (EDJ) surface (in mm^2) to compute both the average enamel thickness (AET) index (the volume of enamel divided by the EDJ surface; index in millimeters) and the relative enamel thickness (RET) index (the AET index divided by the cubic root of dentine volume; a scale-free index).

For root analysis, we followed procedures provided by Kupczik and Hublin⁶⁶. Six measurements were taken (SI 3 Fig. 2): root length (from the cervical plane to the apex of the root); total root volume (the volume of the root below the cervical plane, including dentine and pulp); pulp volume; coronal pulp volume (the portion of the pulp above the cervical plane); root pulp volume (the portion of the pulp below the cervical plane); and cervical plane area (the area of the tooth section obtained by sectioning the cervical plane).

Dental tissue data and root metrics computed for EQH2 were compared to a hominin sample that underwent micro-CT scanning at the Max Planck Institute for Evolutionary Anthropology, at a resolution ranging from 12.58 to 30.19 μm . The hominin sample consisted of M^3 teeth from *H. heidelbergensis*, Neandertals, early *H. sapiens*, Upper Palaeolithic *H. sapiens*, and recent *H. sapiens* (SI 3 Table 3).

Standardized scores (z scores) were computed to establish which group's mean (Neandertals, early and Upper Palaeolithic *H. sapiens*, or recent *H. sapiens*) the RET index and root metrics of EQH2 were closest to (SI 3 Table 4). Finally, we used a leave-one-out cross-validation linear discriminant analysis (LDA) of root metrics to assign the specimen to the group with the highest posterior probability.

For data processing and analyses, we used R software v. 2.15.1⁶⁷.

EQH3. Femoral and tibial length dimensions were obtained with a sliding caliper and osteometric board. For angular measurements, we used a goniometer (SI 4 Tables 1, 2; SI 4 Figs 1,2). Osteological measurements follow those defined by Martin⁶⁸ and other scholars^{35,36,69}. The bones were scanned on a medical CT scanner at standard medical calibration (120 kV; 0.5 mm thick layers) at the Sheba Medical Center in Israel. The total cross-sectional area and total cross-sectional area of the cortical bone were measured at the reformatted horizontal plane of the femoral midshaft. The illustrations of the midshaft cross sections that appear in Fig. 4D,E,F (below the photographs) are based on the horizontal reformatted cross sections of the three bones. A specialist in pediatric radiology (MS) identified the epiphyseal line on the CT scans and noted the presence and absence of pathologies.

The results for EQH3 were compared to those for recent *H. sapiens*, early *H. sapiens*, and *H. neanderthalensis*, taken from published data (for example, refs 35 and 36; see SI 4 Tables 3,4). Well-established morphological differences between the femur and tibia of Neandertals and *H. sapiens* enabled us to identify EQH3 as a Neandertal (SI 4). Age estimation was based on the stage of epiphyseal union, bone length, and age-related pathology (osteoarthritis) (SI 4). We determined gender on the basis of morphological differences between male and female Neandertals (SI 4 Table 5)^{33,69}. The stature estimation was based on 11 formulas: three formulas use femur length, four use tibial length, and four use femoral and tibial length (SI 4 Table 6). EQH3's stature was compared to that of recent *H. sapiens*, early *H. sapiens*, *H. neanderthalensis*, and the Sima de los Huesos hominins (SI 4 Table 7).

References

- Shea, J. J. The Middle Paleolithic of the East Mediterranean Levant. *J. World Prehist.* **17**, 313–394, doi:10.1023/B:JOWO.0000020194.01496.fe (2003).
- Hovers, E. Neandertals and modern humans in the Middle Paleolithic of the Levant: What kind of interaction? *When Neandertals and Moderns Met*, (ed. Conard, N.) 65–86 (Kerns Verlag, Tübingen, 2006).
- Valladas, H. *et al.* Thermoluminescence dates for the Neanderthal burial site at Kebara in Israel. *Nature* **330**, 150–160, doi:10.1038/330159a0 (1987).
- Valladas, H. *et al.* Thermoluminescence dating of Mousterian 'Proto-Cro-Magnon' remains from Israel and the origin of Modern Man. *Nature* **331**, 614–616, doi:10.1038/331614a0 (1988).
- Valladas, H., Mercier, N., Joron, J. L. & Reyss, J. L. GIF Laboratory dates for Middle Paleolithic Levant. *Neandertals and Modern Humans in Western Asia*, (eds Akazawa, T., Aoki, K., Bar-Yosef, O.) 69–76 (Plenum Press, New York, 1998).
- Valladas, H. *et al.* TL Dates for the Neanderthal site of Amud Cave, Israel. *J. Archaeol. Sci.* **26**, 259–268, doi:10.1006/jasc.1998.0334 (1999).
- Bar-Yosef, O. & Callander, J. The woman from Tabun: Garrod's doubts in historical perspective. *J. Hum. Evol.* **37**, 879–885, doi:10.1006/jhev.1999.0368 (1999).
- Grün, R. & Stringer, C. B. Tabun Revisited: Revised ESR Chronology and New ESR and U-series Analyses of Dental Material from Tabun C1. *J. Hum. Evol.* **39**, 601–612, doi:10.1006/jhev.2000.0443 (2000).
- Stringer, C. B., Grün, R., Schwarcz, H. P. & Goldberg, P. ESR dates for the hominid burial site of Es Skhul in Israel. *Nature* **338**, 756–758, doi:10.1038/338756a0 (1989).
- Mercier, N. *et al.* Thermoluminescence date for the Mousterian burial site of Es-Skhul, Mt. Carmel. *J. Archaeol. Sci.* **20**, 169–174, doi:10.1006/jasc.1993.1012 (1993).
- Mercier, N. & Valladas, H. Reassessment of TL age estimates of burnt flints from the Paleolithic site of Tabun Cave, Israel. *J. Hum. Evol.* **45**, 401–409, doi:10.1016/j.jhevol.2003.09.004 (2003).
- Coppa, A., Grün, R., Stringer, C., Eggins, S. & Vargiu, R. Newly recognized Pleistocene human teeth from Tabun Cave, Israel. *J. Hum. Evol.* **49**, 301–315, doi:10.1016/j.jhevol.2005.04.005 (2005).
- Coppa, A., Manni, F., Stringer, C., Vargiu, R. & Vecchi, F. Evidence for new Neanderthal teeth in Tabun Cave (Israel) by the application of self-organizing maps (SOMs). *J. Hum. Evol.* **52**, 601–613, doi:10.1016/j.jhevol.2006.11.009 (2007).
- Bosch, M. D. *et al.* New chronology for Ksar 'Akil (Lebanon) supports Levantine route of modern human dispersal into Europe. *Proc. Natl. Acad. Sci. USA* **112**, 7683–7688, doi:10.1073/pnas.1501529112 (2015).
- Hovers, E. *The Lithic Assemblages of Qafzeh Cave*. (Oxford University Press, Oxford, 2009).
- Hershkovitz, I. *et al.* Levantine cranium from Manot Cave (Israel) foreshadows the first European modern humans. *Nature* **520**, 216–219, doi:10.1038/nature14134 (2015).

17. Kuhlwilm, M. *et al.* Ancient gene flow from early modern humans into Eastern Neanderthals. *Nature* **530**, 429–433, doi:10.1038/nature16544 (2016).
18. Fu, Q. *et al.* Genome sequence of a 45,000-year-old modern human from western Siberia. *Nature* **524**, 216–219 (2014).
19. Hovers, E. & Belfer-Cohen, A. On variability and complexity: lessons from the Levantine Middle Paleolithic record. *Curr. Anthropol.* **54**(S8), S337–S357, doi:10.1086/673880 (2013).
20. Groucutt, H. S. *et al.* Stone tool assemblages and models for the dispersal of Homo sapiens out of Africa. *Quat. Int.* **382**, 8–30, doi:10.1016/j.quaint.2015.01.039 (2015).
21. McCown, T. D. & Keith, A. *The Stone Age of Mount Carmel II*. (Clarendon Press, Oxford, 1939).
22. Rak, Y. Does any Mousterian cave present evidence of two hominid species? *Neanderthals and Modern Humans in Western Asia*, (eds Akazawa, T., Aoki, K., Bar-Yosef, O.) 353–366 (Plenum Press, New York, 1998).
23. Sharon, G., Zaidner, Y. & Hovers, E. Opportunities, problems and future directions in the study of open air Middle Paleolithic sites. *Quat. Intern.* **331**, 1–5, doi:10.1016/j.quaint.2014.03.055 (2014).
24. Hovers, E., Malinsky-Buller, A., Ekshtain, R., Oron, M. & Yeshurun, R. 'Ein Qashish—a new open air Middle Paleolithic site in northern Israel. *J. Israel. Prehist. Soc.* **38**, 7–40 (2008).
25. Hovers, E. *et al.* Islands in a stream? Reconstructing site formation processes in the late Middle Paleolithic site of 'Ein Qashish, northern Israel. *Quat. Intern.* **331**, 216–233, doi:10.1016/j.quaint.2014.01.028 (2014).
26. Greenbaum, N., Ekshtain, R., Malinsky-Buller, A., Porat, N. & Hovers, E. The stratigraphy and paleogeography of the Middle Paleolithic open air site of 'Ein Qashish, Northern Israel. *Quat. Intern.* **331**, 203–215, doi:10.1016/j.quaint.2013.10.037 (2014).
27. Ekshtain, R., Malinsky-Buller, A., Ilani, S., Segal, I. & Hovers, E. Raw material exploitation around the Middle Paleolithic site of 'Ein Qashish. *Quat. Intern.* **331**, 248–266, doi:10.1016/j.quaint.2013.07.025 (2014).
28. Malinsky-Buller, A., Ekshtain, R. & Hovers, E. Organization of lithic technology at 'Ein Qashish, a late Middle Paleolithic open air site in Israel. *Quat. Intern.* **331**, 234–247, doi:10.1016/j.quaint.2013.05.004 (2014).
29. Barzilai, O., Ekshtain, R., Malinsky-Buller, A. & Hovers, E. 'En Qashish ('Ein Qashish). *Hadashot Arkheologiot* **127** (2015) <http://www.hadashot-esi.org.il>.
30. Molnar, S. Human tooth wear, tooth function and cultural variability. *Am. J. Phys. Anthropol.* **34**, 175–190, doi:10.1002/ajpa.1330340204 (1971).
31. Boule, M. *L'homme fossile de La Chapelle-aux-Saints* (Vol. 6) (Masson, 1913).
32. Trinkaus, E. The evolution of the hominid femoral diaphysis during the Upper Pleistocene in Europe and the Near East. *Zeitschrift für Morphologie und Anthropologie* 291–319 (1976).
33. Trinkaus, E. *The Shanidar Neanderthals* (Academic Press, New York, 1983).
34. Heim, J. L. Les Hommes Fossiles de La Ferrassie. Tome II. Les Squelettes adultes (squelette de membres). *Arch. Inst. Paléontol. Humaine.* **38** (1982).
35. Shackelford, L. L. & Trinkaus, E. Late Pleistocene human femoral diaphyseal curvature. *Am. J. Phys. Anthropol.* **118**, 359–370, doi:10.1002/ajpa.10093 (2002).
36. De Groote, I. Femoral curvature in Neanderthals and modern humans: a 3D geometric morphometric analysis. *J. Hum. Evol.* **60**, 540–548, doi:10.1016/j.jhevol.2010.09.009 (2011).
37. Lovejoy, C. O. & Trinkaus, E. Strength and robusticity of the Neanderthal tibia. *Am. J. Phys. Anthropol.* **53**, 465–470, doi:10.1002/(ISSN)1096-8644 (1980).
38. Stringer, C. B., Trinkaus, E., Roberts, M. B., Parfitt, S. A. & Macphail, R. I. The middle Pleistocene human tibia from Boxgrove. *J. Hum. Evol.* **34**, 509–547, doi:10.1006/jhev.1998.0215 (1998).
39. Trinkaus, E. & Ruff, C. B. Diaphyseal cross-sectional geometry of Near Eastern Middle Palaeolithic humans: the femur. *J. Archaeol. Sci.* **26**, 409–424, doi:10.1006/jasc.1998.0343 (1999).
40. Carretero, J. M. *et al.* Stature estimation from complete long bones in the Middle Pleistocene humans from the Sima de los Huesos, Sierra de Atapuerca (Spain). *J. Hum. Evol.* **62**, 242–255, doi:10.1016/j.jhevol.2011.11.004 (2012).
41. O'Connor, J. E., Bogue, C., Spence, L. D. & Last, J. A method to establish the relationship between chronological age and stage of union from radiographic assessment of epiphyseal fusion at the knee: an Irish population study. *J. Anatom.* **212**, 198–209, doi:10.1111/joa.2008.212.issue-2 (2008).
42. Dogaroiu, C. & Avramoiu, M. Correlation between chronological age and the stage of union of the distal femur and proximal tibia epiphyses in a Romanian sample population. *Rom. J. Leg. Med.* **23**, 171–176, doi:10.4323/rjlm (2015).
43. Zions, L.E. Fractures and dislocations about the knee. *Skeletal Trauma in Children 3rd ed.* 439–471 (Philadelphia, PA: Saunders, 2003).
44. Swartz, S. M. The functional morphology of weight bearing: limb joint surface area allometry in anthropoid primates. *J. Zool* **218**, 441–460, doi:10.1111/jzo.1989.218.issue-3 (1989).
45. Kadowaki, S. Issues of Chronological and Geographical Distributions of Middle and Upper Palaeolithic Cultural Variability in the Levant and Implications for the Learning Behavior of Neanderthals and Homo sapiens. *Dynamics of Learning in Neanderthals and Modern Humans Volume 1: Cultural Perspectives, Replacement of Neanderthals by Modern Humans Series* (eds Akazawa, T. *et al.*) 59–91, doi:10.1007/978-4-431-54511-8_4 (Springer Japan, 2013).
46. Sharon, G. & Oron, M. The lithic tool arsenal of a Mousterian hunter, *Quarter. Intern.* **331**, 167–185, doi:10.1016/j.quaint.2013.10.024 (2014).
47. Ziaei, M., Schwarcz, H. P., Hall, C. M. & Grün, R. Radiometric dating of the Mousterian site at Quneitra. *Quneitra: A Mousterian Site on the Golan Heights*. 232–235 (The Hebrew University, Jerusalem, 1990).
48. Guipert, G., de Lumley, M. A., Tuffreau, A. & Mafart, B. A late Middle Pleistocene hominid: Biache-Saint-Vaast 2, north France. *CR Palevol.* **10**, 21–33, doi:10.1016/j.crpv.2010.10.006 (2010).
49. Faivre, J. P. *et al.* Middle Pleistocene Human Remains from Tourville la Rivière (Normandy, France) and Their Archaeological Context. *PLoS ONE* **9**(10), e104111, doi:10.1371/journal.pone.0104111 (2014).
50. Belfer-Cohen, A. & Hovers, E. In the eye of the beholder: Mousterian and Natufian burials in the Levant. *Curr. Anthropol.* **33**, 463–467, doi:10.1086/204098 (1992).
51. Gargett, R. H. Grave shortcomings: the evidence for neanderthal burial. *Curr. Anthropol.* **30**, 157–190, doi:10.1086/203725 (1989).
52. Gargett, R. Middle Palaeolithic burial is not a dead issue: The view from Qafzeh, Saint-Césaire, Kebara, Amud, and Dederiyeh. *J. Hum. Evol.* **37**, 27–90, doi:10.1006/jhev.1999.0301 (1999).
53. Hovers, E., Kimbel, W. H. & Rak, Y. Amud 7—still a burial. Response to Gargett. *J. Hum. Evol.* **39**, 253–260, doi:10.1006/jhev.1999.0406 (2000).
54. Zilhão, J. Lower and Middle Palaeolithic mortuary behaviours and the origins of ritual burial. *Death Rituals, Social Order and the Archaeology of Immortality in the Ancient World. 'Death Shall Have No Dominion'* (eds Renfrew, C., Boyd, M. J., Morley, I.) 27–44 (Cambridge University Press, 2015).
55. Rendu, W. *et al.* Evidence supporting an intentional Neanderthal burial at La Chapelle-aux-Saints. *Proc. Natl. Acad. Sci. USA* **111**, 80–86, doi:10.1073/pnas.1316780110 (2014).
56. Dibble, H. L. *et al.* A critical look at evidence from La Chapelle-aux-Saints supporting an intentional Neanderthal burial. *J. Archaeol. Sci.* **53**, 649–657, doi:10.1016/j.jas.2014.04.019 (2015).
57. Henry, D. O. *et al.* The effect of terrain on Neanderthal ecology in the Levant. *Quat. Int.* doi:10.1016/j.quaint.2015.10.023 (2016).

58. Higgins, R. W. & Ruff, C. B. The effects of distal limb segment shortening on locomotor efficiency in sloped terrain: implications for Neanderthal locomotor behavior. *Am. J. Phys. Anthropol.* **146**, 336–345, doi:10.1002/ajpa.v146.3 (2011).
59. Rak, Y. Morphological variation in *Homo neanderthalensis* and *Homo sapiens* in the Levant: a biogeographical model. *Species, Species Concept and Primate Evolution* (eds Kimbel, W. H. and Martin, L. B.) 523–536 (Plenum Press, New York, 1993).
60. Shea, J. J. Transitions or turnovers? Climatically-forced extinctions of *Homo sapiens* and Neanderthals in the east Mediterranean Levant. *Quat. Sci. Rev.* **27**, 2253–2270, doi:10.1016/j.quascirev.2008.08.015 (2008).
61. Belmaker, M. & Hovers, E. Ecological change and the extinction of the Levantine Neanderthals: implications from a diachronic study of micromammals from Amud Cave, Israel. *Quat. Sci. Rev.* **30**, 3196–3209, doi:10.1016/j.quascirev.2011.08.001 (2011).
62. Speth, J. D. & Clark, J. Hunting and overhunting in the Levantine Late Middle Palaeolithic. *Before Farming* **3**, Article 1 (2006).
63. Hartman, G. *et al.* Isotopic evidence for Last Glacial climatic impacts on Neanderthal gazelle hunting territories at Amud Cave, Israel. *J. Hum. Evol.* **84**, 71–82, doi:10.1016/j.jhevol.2015.03.008 (2015).
64. Hublin, J. J. The modern human colonization of western Eurasia: when and where? *Quat. Sci. Rev.* **118**, 194–210, doi:10.1016/j.quascirev.2014.08.011 (2015).
65. Benazzi, S. *et al.* Technical Note: Guidelines for the Digital Computation of 2D and 3D Enamel Thickness in Hominoid Teeth. *Am. J. Phys. Anthropol.* **153**, 305–313, doi:10.1002/ajpa.22421 (2014).
66. Kupczik, K. & Hublin, J. J. Mandibular molar root morphology in Neanderthals and Late Pleistocene and recent *Homo sapiens*. *J. Hum. Evol.* **59**, 525–541, doi:10.1016/j.jhevol.2010.05.009 (2010).
67. R Development Core Team. R: a language and environment for statistical computing. R Foundation for Statistical Computing, Vienna, Austria. <http://www.r-project.org>. (2012).
68. Martin, R. *Lehrbuch der Anthropologie in Systematischer Darstellung mit Besonderer Berücksichtigung der Anthropologischen Methoden für Studierende, Ärzte und Forschungsreisende* (Zweiter Band: Kraniologie, Osteologie, 2nd ed. Jena, Gustav Fischer, 1928).
69. Trinkaus, E. Sexual differences in Neanderthal limb bones. *J. Hum. Evol.* **9**, 377–397, doi:10.1016/0047-2484(80)90049-4 (1980).

Acknowledgements

The 2013 excavation at 'Ein Qashish (Permit No. A-6866; map ref. 210361–431/732109–147) were directed by E. Hovers and O. Barzilai on behalf of the Hebrew University and the Israel Antiquities Authority. The Cross-Israel Highway financed the excavations. The fieldwork was carried by A. Vered, M. Karkovsky, G. Sovolev, and P. Spivak (area supervision); G. Balan, D. Almog, A. Gottlieb, M. Mor, A. Popdaryavko and L. Panksik (assistant area supervisors); Y. Amrani and E. Bachar (administration); V. Essman and Y. Shmidov (surveying and drafting); M. Olman (field drawings); L. Brilovsky, and H. Goldgeier (field laboratory); A. Gorzalczy, K. Sa'id and L. Talmi (planning and logistics). Michal Birkenfeld and Alon Barash prepared Figure 1. Figure 2 was prepared by Noga Yoselevich, the Cartography Laboratory, The Department of Geography and Environmental Studies, University of Haifa. Stefano Benazzi prepared Figure 3. M. Ullman drew Figure 4a; E. Hovers photographed Figure 4b; Avishag Ginzburg and Alon Barash photographed and prepared Figures 4c – 4f.

Author Contributions

E.B., E.H., S.B., Y.R. and O.B. wrote the main manuscript text. R.E., A.B., S.B., N.P. and O.B. prepared Figures 1–4. E.B., E.H., R.E., A.M.B., N.A., S.B., J.J.H., L.L., N.G., N.M., G.O., N.P., J.R., R.Y., R.S.G., N.N., M.C.S., Y.R. and O.B. performed data collection and analysis. All authors participated in the preparation of the supplementary material and reviewed the manuscript.

Additional Information

Supplementary information accompanies this paper at doi:10.1038/s41598-017-03025-z

Competing Interests: The authors declare that they have no competing interests.

Publisher's note: Springer Nature remains neutral with regard to jurisdictional claims in published maps and institutional affiliations.



Open Access This article is licensed under a Creative Commons Attribution 4.0 International License, which permits use, sharing, adaptation, distribution and reproduction in any medium or format, as long as you give appropriate credit to the original author(s) and the source, provide a link to the Creative Commons license, and indicate if changes were made. The images or other third party material in this article are included in the article's Creative Commons license, unless indicated otherwise in a credit line to the material. If material is not included in the article's Creative Commons license and your intended use is not permitted by statutory regulation or exceeds the permitted use, you will need to obtain permission directly from the copyright holder. To view a copy of this license, visit <http://creativecommons.org/licenses/by/4.0/>.

© The Author(s) 2017

**The first Neanderthal remains from an open-air Middle Palaeolithic site in the
Levant**

Supporting Information

SI 1. 'Ein Qashish: Site Background

SI 2. Optically Stimulated Luminescence (OSL) Dating

SI 3. EQH-2 (Upper Third Molar)

SI 4. Description of the EQH-3 Bones

Ella Been^{1✉,2}, Erella Hovers^{3,4}, Ravid Ekshtain³, Ariel Malinski-Buller⁵, Nuha Agha⁶,
Alon Barash⁷, Daniella E. Bar-Yosef Mayer^{8,9}, Stefano Benazzi^{10,11}, Jean-Jacques
Hublin¹¹, Lihi Levin², Noam Greenbaum¹², Netta Mitki³, Gregorio Oxilia^{13,10}, Naomi
Porat¹⁴, Joel Roskin^{15,16}, Michalle Soudack^{17,18}, Reuven Yeshurun¹⁹, Ruth Shahack-
Gross¹⁵, Nadav Nir³, Mareike C. Stahlschmidt²⁰, Yoel Rak², Omry Barzilai⁶

¹ Department of Physical Therapy, Faculty of Health Professions, Ono Academic
College, Kiryat Ono 55107, Israel

² Department of Anatomy and Anthropology, Sackler Faculty of Medicine, Tel Aviv
University, Tel Aviv 69978, Israel

³ Institute of Archaeology, the Hebrew University of Jerusalem, Jerusalem 91905, Israel

⁴ Institute of Human Origins, P.O. Box 874101, Arizona State University, Tempe AZ
85287-4101 USA

⁵ MONREPOS Archaeological Research Centre and Museum for Human Behavioural
Evolution, Schloss Monrepos D – 56567 Neuwied, Germany

⁶ Israel Antiquities Authority, P.O. Box 586, Jerusalem 91004, Israel

- ⁷ Faculty of Medicine in the Galilee, Bar Ilan University, Zefat 13115, Israel
- ⁸ Steinhardt Museum of Natural History, Tel Aviv University, Tel Aviv 69978, Israel
- ⁹ Peabody Museum of Archaeology and Ethnology, Harvard University, 11 Divinity Avenue Cambridge MA 02138, USA
- ¹⁰ Department of Cultural Heritage, University of Bologna, Via degli Ariani 1 48121 Ravenna, Italy
- ¹¹ Department of Human Evolution, Max Planck Institute for Evolutionary Anthropology, Deutscher Platz 6 04103 Leipzig, Germany
- ¹² Department of Geography & Environmental Studies, University of Haifa, Haifa 3498838, Israel
- ¹³ Department of Biology, University of Florence, Via del Proconsolo, 12 50122 Firenze, Italy
- ¹⁴ Luminescence Dating Lab, Geological Survey of Israel, Jerusalem 95501, Israel
- ¹⁵ Department of Maritime Civilizations, University of Haifa, Haifa 3498838, Israel
- ¹⁶ School of Sciences, Achva Academic College, Shikmim Mobile Post 79800, Israel
- ¹⁷ Department of Diagnostic Imaging, Chaim Sheba Medical Center, Tel Hashomer 52621, Israel
- ¹⁸ Sackler Faculty of Medicine, Tel Aviv University, Tel Aviv 69978, Israel
- ¹⁹ Zinman Institute of Archaeology, University of Haifa, Haifa 3498838, Israel
- ²⁰ School of Archaeology, University College Dublin, Belfield Dublin 4, Ireland

SI 1. 'Ein Qashish: Site Background

The site complex of 'Ein Qashish is located in the Jezreel Valley, ca. 100 m south of the Qishon stream and south of Tel Qashish (SI 1 Fig.1). The site was discovered in a 2004 survey by the Israel Antiquities Authority (IAA). It was excavated during 2005 (24), and again during 2009, 2010 and 2011, by the Hebrew University of Jerusalem (HUI) (25). The excavations revealed remains of a late Mousterian campsite dated to 70,000–60,000 years ago (26–28). A nearly complete horned skull of an auroch (*Bos primigenius*) was found associated with flint tools during this excavation. Deposition of artefacts and bones was partially secondary, and the original position of the site was hypothesized, on the basis of lithic taphonomy and geomorphological considerations, to be 40–50 m south-southwest of the excavation area (25).

In preparation for the extension of a major highway in the region, archaeological prospection was carried out by the IAA in the site's vicinity to determine its potential and decide on excavation plans. Mechanical test trenches were dug in 2012 to estimate the size of the site (29). The trenches revealed that the Middle Palaeolithic site extended over an area of more than 1400 m² (SI 1 Fig. 1). Notably, a nondiagnostic fragment of a human skull was recovered from the base of Trench 5 in waterlogged sediments corresponding to geological Layer 1 (SI 1 Fig. 1).

Accidental damage to the site led to a large-scale salvage excavation in the summer of 2013. The excavation, a collaboration between the HUI and the IAA, was conducted in six Areas (A–F), totaling ~650 m² (SI 1 Fig. 2). All the areas were excavated according to a single grid system and aligned to the Israel Grid System coordinates.

All artefacts larger than 20 mm were measured three-dimensionally using Total Station instruments (Sokkia 630 and FTD 05). Other artefacts were collected and bagged according to 50 × 50 cm subsquares and 5 cm spits. All the sediments were dry-sieved and 10–15% were wet-sieved.

Stratigraphy and Sedimentology

The sedimentary sequence exposed in the 2013 excavation was tentatively correlated to a sedimentary sequence documented in geological trenches dug in 2012 (Greenbaum, pers. obs.), which included six layers (Fig. 2). The two lowermost layers were not exposed in the current excavation; thus, the site's sequence begins with Layer 3.

In general, sediments in all layers are dominated by clay but contain also silt and fine sand, rich in quartz. Layer 3 is very rich in stone and bone artefacts, including the remains of EQH-3 in Layer 3b. The layer is composed of dark black, clay-rich sediment (Layer 3a) that grades vertically into gray-black, clay-rich sediment (Layer 3b). The sedimentary layer has abundant slickensides and metallic gley along cracks. This field appearance indicates hydromorphic reducing conditions. In addition, this layer includes fossilized roots and rootlets (rhizoliths), gypsum crystals, occasional calcite veins along cracks, and cobbles from local geological formations. These indicate that the sediments were previously exposed long enough to allow for plant growth (rhizoliths) and evaporation (gypsum), i.e., a habitat conducive to human activity.

Infrared, x-ray fluorescence (XRF), and inductively coupled plasma (ICP) mass spectrometry analyses of minerals and elements in animal bones from this unit

show an abundance of iron and manganese oxides. These often appear as dark or reddish-orange coats on and within the bones. Bone mineral crystallinity was evaluated using the infrared splitting factor method. Values measured in 84 samples of animal bones average 3.4 ± 0.2 , indicating moderately well preserved bone mineral. The human femur bone mineral crystallinity falls within the same range. All the bones are devoid of collagen (70).

Layer 3 grades into the overlying Layer 4, a reddish brown, clay-rich unit up to ca. 50 cm thick that contains rhizoliths and gypsum crystals. The spatial extent of this unit is more confined than that of the underlying and overlying layers, and Middle Palaeolithic (MP) artefacts are fewer.

The Archaeological Context of the Hominin Finds

Area A, where specimen EQH-2 was found, is situated ca. 30 m west of the area of the excavations carried out during the years 2009, 2010, and 2011, and it may represent the original locality from where the finds were fluvially transported (25). Forty-two m² were excavated in this area, exposing two Middle Palaeolithic layers: Layer 5a, 60–90 cm thick, and Layer 5b, 50–70 cm thick. Both layers were cut at the northeastern corner of the area by a Holocene fluvial channel (29). The finds from Layer 5b are abundant and consist of fresh, sharp flint items in a variety of sizes, as well as fragments of animal bones and teeth belonging to large herbivores, mainly auroch. The flint assemblage from this layer is characterized by large primary items showing the initial stages of the knapping sequences. Twenty-one aggregates containing 51 artefacts have been identified so far (work in progress), showing several reduction sequences (SI 1 Fig. 3). Refits from one aggregate were found at maximum

vertical distances of 50 cm and maximum horizontal distances of 4 m, suggesting limited postdepositional vertical dispersion. EQH-2 was found in Layer 5a, which yielded fewer finds than its overlying layer, 5b. Lithic production technology was the same as in Layer 5b.

Area B is situated at the northwestern part of the excavation plot. Ca. 45 m² were excavated, exposing a well-preserved horizon ca. 20–40 cm thick (Layer 3b). Specimen EQH-3 was found in this layer (SI 1 Fig. 4), which also contained many flint items (mostly in fresh condition with only a few abraded or patinated), fragmented animal bones, ochre, a complete antler of a roe deer, and a marine mollusk from the Mediterranean Sea, *Hexaplex trunculus* (Linnaeus, 1758) (SI 1 Fig. 5a). Among the large angular cobbles found embedded in the clay were three modified stones that might have functioned as anvils (detailed analysis and residue analysis are in progress) (SI 1 Fig. 5b). These items were found at 22.25–22.20 m above mean sea level, at the same elevation as the EQH-3 bones but several meters from them.

Preliminary refitting efforts in Area B have so far resulted in 4 aggregates composed of 21 flint pieces. Of these, 8 aggregates derive from an artefact concentration in squares L44–L45, at an elevation of 21.96–22.08 m (ca. 3 m north of the remains of EQH-3), with little horizontal (up to 1 m) or vertical (up to 12 cm) movement. The additional aggregate of 2 pieces in squares I41–J41, 21.83–21.86 also shows little horizontal (1 m) or vertical movement (3 cm).

Lithics

All the lithic artefacts from the 2013 excavation were assigned to the Middle Palaeolithic. The densities of lithic artefacts in the various excavation areas differ and may correspond to differences in depositional and postdepositional conditions. The technological makeup of the lithic assemblages is similar, including the Levallois component (SI 1 Fig. 6). The frequencies of Levallois flaking are similarly low in all the excavated areas, a pattern known in many Levantine open-air sites (15 and references therein).

Fauna

A preliminary count and analysis of specimens identifiable to the genus or species level ($n = 87$) yielded a medium-sized faunal assemblage completely dominated by ungulates; additionally, more than 200 faunal specimens were identified to the level of anatomical part and body-size class. No small game or carnivore skeletal elements were found. The most frequent species is the auroch (*Bos primigenius*), followed by the mountain gazelle (*Gazella gazella*), Mesopotamian fallow deer (*Dama mesopotamica*), equid (*Equus* sp.), wild boar (*Sus scrofa*), and roe deer (*Capreolus capreolus*). The excavations of 2009, 2010, and 2011 yielded a similar faunal spectrum, dominated by auroch, Mesopotamian fallow deer, and mountain gazelle (25).

Differences were noted in the density of the faunal remains and in their degree of breakage and abrasion within the excavation areas. Most notable were the differences in the density, breakage, and abrasion of remains in Area C, which yielded only a handful of small, weathered fragments, and Areas B and F, which included hundreds of well-preserved, identifiable bones. Some between-area differences were

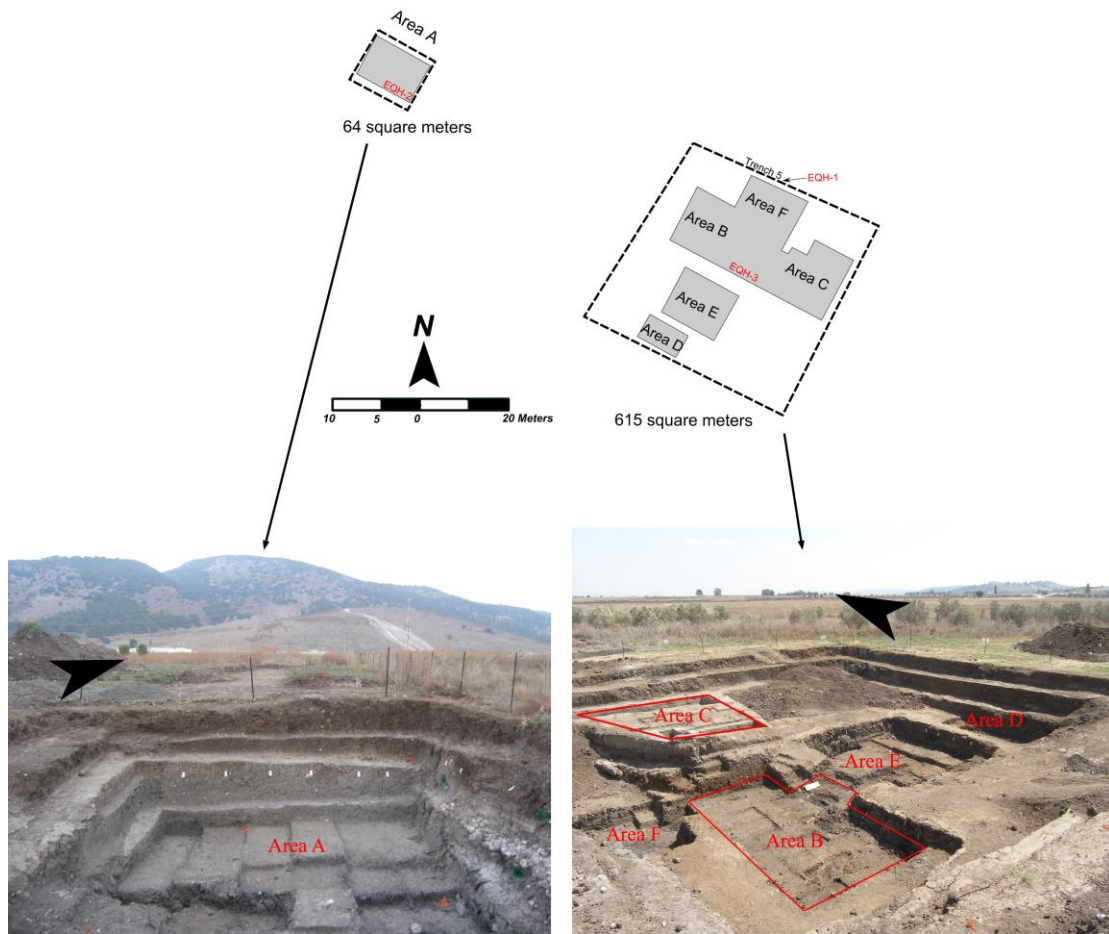
noted in the taxonomic spectrum, specifically the dominance of auroch in Area A and the more even representation of the three major ungulate species in Area B.

Skeletal parts rich in meat, such as upper limb bones, were found in all the excavation areas. Virtually all the limb bones are fragmented, and some show cut marks, typical of meat filleting, as well as hammerstone percussion marks (SI 1 Fig. 7). This indicates that human agents were responsible for the deposition of the animal remains, most probably the result of hunting.

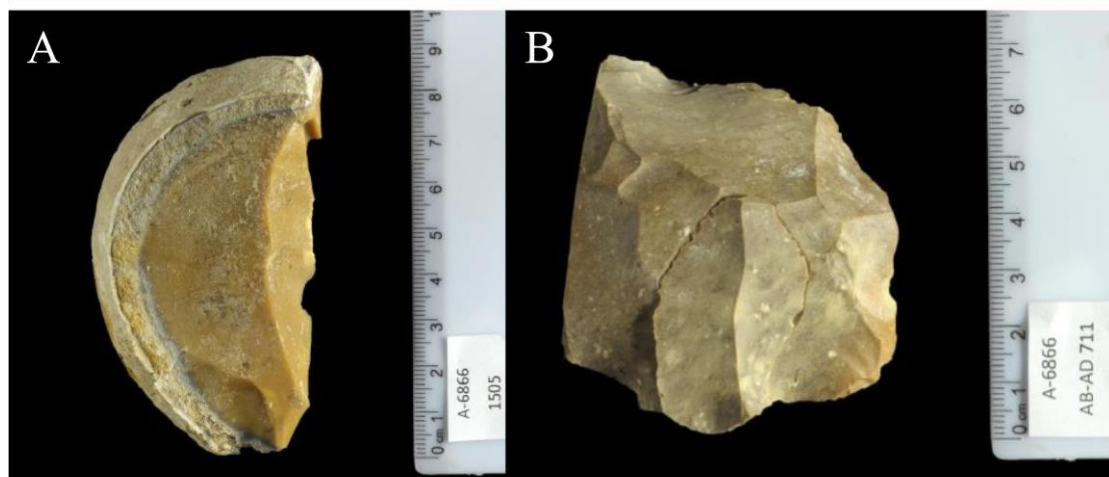
SI 1 Figures



SI 1 Fig. 1. The 2013 excavation at 'Ein Qashish (area under the shade cloth). Locations of the 2009–2011 excavations, and of the 2012 mechanical trenches (in green). The estimated area of the site (dotted red circle) and the location of EQH-1 are indicated.

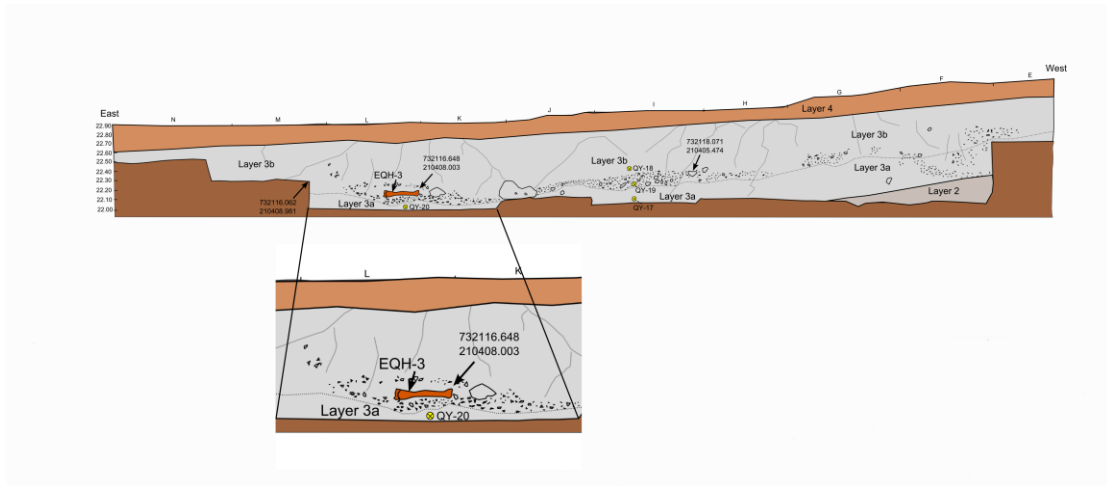


SI 1 Fig. 2. The excavation areas in 'Ein Qashish (2013).

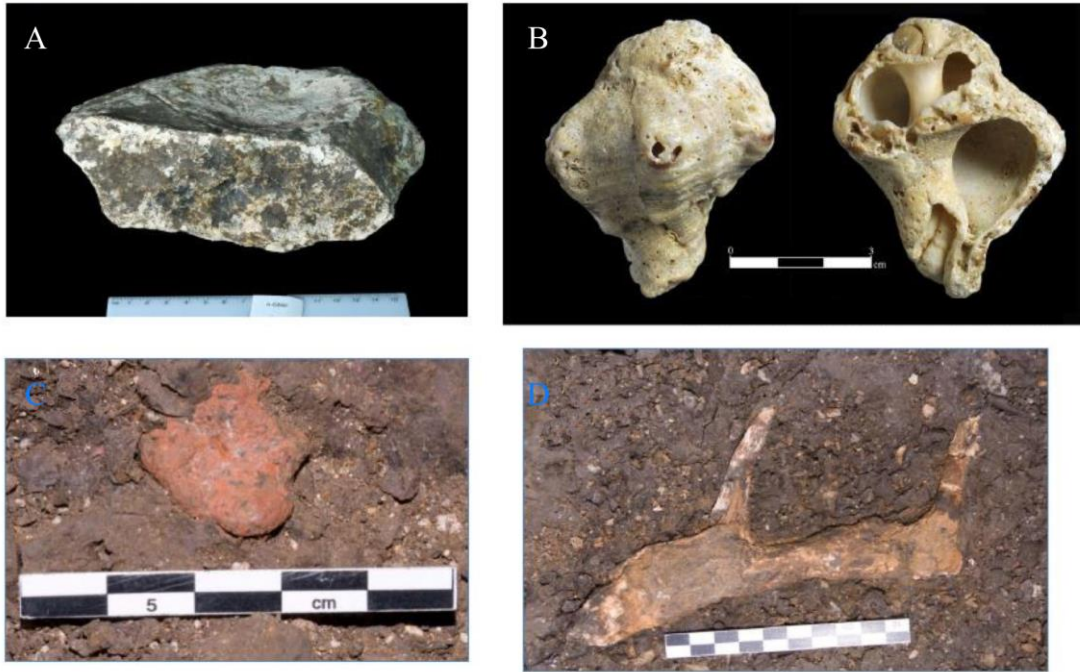


SI 1 Fig. 3. Flint artefacts from Area A. (A) A large flake with cortex. (B) A refitted flint aggregate.

Photo Clara Amit, Courtesy of the Israel Antiquities Authority

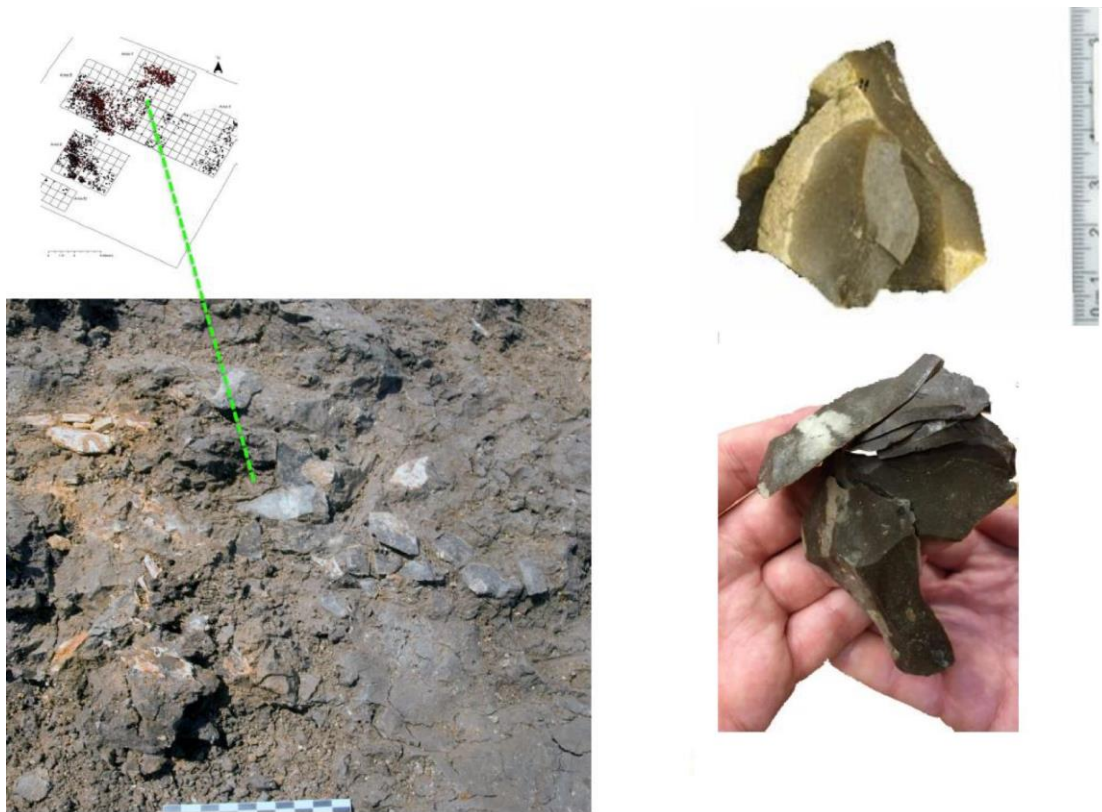


SI 1 Fig. 4. A section showing the sedimentological context of EQH-3 (top), and a close-up of its stratigraphic position (inset at bottom).



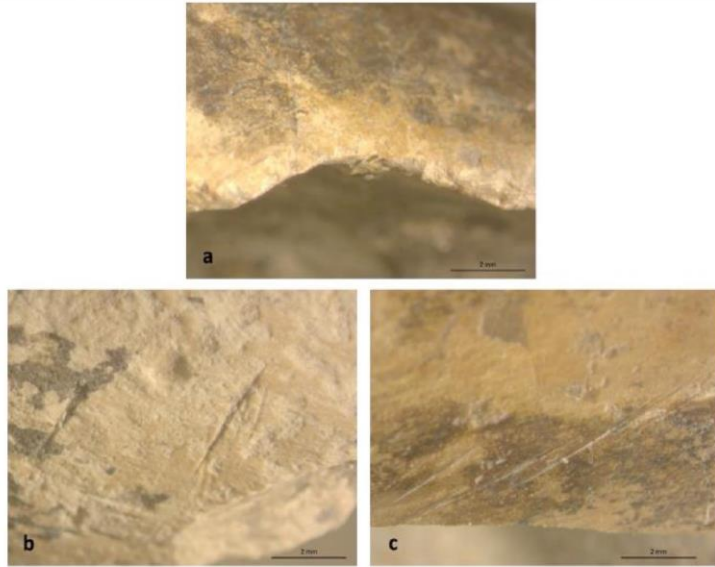
SI 1 Fig. 5. Finds from Layer 3b in Area B. (A) Stone manuport. (B) *Hexaplex trunculus* (Linnaeus, 1758) shell. (C) Ochre. (D) An antler of a roe deer.

Photo (A, B) Clara Amit, Courtesy of the Israel Antiquities Authority



SI 1 Fig. 6. Refitted aggregates from Area B. Refits are laterally and vertically clustered (lower right).

Photo (Top right) Clara Amit, Courtesy of the Israel Antiquities Authority



SI 1 Fig. 7. Examples of butchery at ‘Ein Qashish. (a) Medium ungulate (*Dama mesopotamica*) humerus (#2309) bearing hammerstone percussion signs (the conchoidal notch). (b) Large ungulate (*Bos primigenius*) radius (#1063) bearing filleting marks. (c) Medium ungulate (*Dama mesopotamica*) tibia (#1731) bearing filleting marks.

SI 2. Optically Stimulated Luminescence (OSL) Dating

The site sequence of the 2013 excavation was dated through optically stimulated luminescence. After site stratigraphy was established, samples were collected from freshly cleaned sections in the different excavation areas. We collected the samples under cover to prevent any exposure to sunlight and then stored them immediately in black, light-tight bags. We took a complementary sample from the same location for dose rate measurements. Several samples were collected from each of the stratigraphic layers exposed in the different sections.

Quartz in the range of 88-125 μm was extracted and measured under suitable dim orange light using routine laboratory procedures (71). After the sediment sample was sieved to the selected grain size, carbonates were dissolved by soaking in 8% HCl followed by rinsing and drying. Heavy minerals and most feldspars were removed using the Frantz magnetic separator, and HF (40%) etching for 40 min was used to dissolve the remaining feldspars and etch the quartz. The samples were then rinsed in 16% HCl overnight to dissolve any fluorides that may have precipitated.

We measured equivalent doses (D_e) for each sample on 17 to 23 aliquots prepared with 1 or 2 mm masks, using a modified single aliquot regenerative (SAR) protocol (72), and we calculated averages and errors using the central age model (CAM) (73). Measurements were carried out on Risø TL/OSL readers (models DA-12 or DA-15). Dose recovery tests over a range of preheats showed that a dose recovery of 100% can be obtained using a preheat of 10 s at 260°C, a test dose of ~9.3 Gy, and a test dose preheat of 5 s at 240°C. These measurement conditions were used throughout.

Alpha, beta, and gamma dose rates were calculated from the concentrations of the radioactive elements measured by inductively coupled plasma (ICP) mass spectrometry (U and Th) or ICP atomic emission spectroscopy (K), using attenuation factors from (74). Cosmic dose rates were estimated from current burial depths, and water content was measured immediately after sampling (SI 2 Table 1).

To identify the most dominant age components in samples with scattered D_e values, we measured single grains from several samples. The data was processed and reliable grains were selected using criteria as in (75). The main age component was isolated using the finite mixture model (FMM) (74).

All samples show good performance with respect to OSL properties and D_e measurements: the OSL signal was bright and decayed rapidly to background levels, indicating a dominant fast component. Recycling ratios were within 8% of unity, indicating that the SAR protocol corrects appropriately for sensitivity changes, and IR signals were negligible. Dose distributions were mostly normal, with overdispersion values (an indication of scatter beyond that expected from the physical measurements) usually less than 25%.

The ages ranged from 9 ka at the top of the sequence to 70–75 ka at the base of the exposed layers (SI 2 Table 1; Fig. 2A). Once preliminary ages were available, it became apparent that samples EQHD-42, EQHD-44, EQHD-46, and EQHD-47 did not conform to the stratigraphic order. (These samples are indicated in SI 2 Fig. 1 as open squares and highlighted in gray in SI 2 Table 1.) Repeated analysis was carried out to ascertain that the D_e values and dose rates were measured correctly. While the D_e values resembled those of nearby samples (from the same unit or section; SI 2 Table 1), the dose rates for three of the four outlier samples were either much higher

(sample EQHD-42) or much lower (samples EQHD-44 and EQHD-46) than the mean dose rate calculated from all samples, 1.55 ± 0.32 Gy/ka.

The lower dose rates could have been caused by dilution with a low-dose-rate mineral, such as calcium carbonate (CaCO_3). The higher dose rates could have resulted from high concentrations of clay or heavy minerals. The carbonate contents were thus measured for these outliers, and for 8 additional samples collected for OSL dating from several sections (SI 2 Table 1). The carbonate content for most samples turned out to be in the range of 1–5%, whereas for one of the outlier samples (EQHD-44) it was 43.8%. Thus, the high carbonate content could explain the low dose rate of that particular sample. Since the resulting age is overestimated, dose rates might have been lowered in more recent times by the deposition of carbonates, and current dose rates do not represent the time-averaged dose rate for this sample over its geological history. However, the deposition of carbonates could not be the reason for the low dose rate in two additional samples, as their carbonate content is not high.

We also wanted to check whether the ages calculated for these samples using the site-averaged dose rate are more concordant and agree better with the stratigraphy. SI 2 Table 2 lists these outlying samples, showing their OSL age against the age expected from nearby samples (either from the same unit in other sections, or from the over- and underlying samples). The ages for these samples were recalculated using the averaged dose rates for the entire site (1.55 Gy/ka). For all four samples, the recalculated ages agree much better with the expected ages, further indicating perturbation in the dose rates of individual samples in rather recent times.

However, we did not find satisfactory clues for changes in dose rates over time for samples other than EQHD-44, and they were not included in further analyses.

SI 2 Fig. 1 shows the ages with their associated errors by stratigraphic layer. Aside from the outliers, the ages fall within range of 74 ka to 59 ka (solid squares). The stars indicate the stratigraphic locations of EQH-2 (a tooth) and EQH-3 (lower limb bones).

To obtain robust ages for individual layers and obtain a chronological framework for the site, ages from each layer across the sections were averaged, excluding the outliers; these averages are presented in Fig. 2A. SI 2 Table 3 lists the samples used to calculate the average for each layer, and its averaged age. Only one sample was collected from Layer 5b: sample EQHD-44 (marked with an asterisk), which turned out to be one of the outliers. As this was the only sample whose low dose rate could clearly be explained by a substantial addition of carbonates at a late stage in the sample's history, here we used the age calculated from the site-averaged dose rate (SI 2 Table 2).

Note the robust ages calculated for Layer 3a, for Layer 3b (where the hominin remains of EQH-3 were found), and for Layer 5a (where the tooth specimen EQH-2 was found). These ages bracket the time of the human remains to 66–68 ka. Note also that OSL dating cannot distinguish clearly between the ages of the lowermost and uppermost Middle Palaeolithic layers (1–5), and it appears that the sediments were deposited rapidly.

SI 2 Tables and Figures

SI 2 Table 1. Field and laboratory data for OSL samples with ages.

| Lab code | Field number | Layer | Area | Depth (m) | Water content (%) | K (%) | U (ppm) | Th (ppm) | Ext. α ($\mu\text{Gy/a}$) | Ext. β ($\mu\text{Gy/a}$) | Ext. γ ($\mu\text{Gy/a}$) | Cosmic ($\mu\text{Gy/a}$) | Total dose ($\mu\text{Gy/a}$) | No. aliquots | OD (%) | D_e (Gy) | CAM Age (Ka) | CaCO_3 (%) |
|---------------|--------------|-------|--------|-----------|-------------------|-------|---------|----------|------------------------------------|-----------------------------------|------------------------------------|-----------------------------|---------------------------------|------------------|----------|----------------------------|--|---------------------|
| EQHD-12 | EQ5-U5 | 5a | T-EQH5 | 2.5 | 12.3 | 0.30 | 1.2 | 4.5 | 6 | 415 | 368 | 154 | 944 \pm 28 | 22/22 | 32 | 61 \pm 3 | 65\pm3 | |
| EQHD-13 | EQ5-U4 | 4 | T-EQH5 | 3.0 | 35.8 | 1.08 | 2.3 | 12.6 | 11 | 953 | 796 | 145 | 1905 \pm 52 | 20/20 | 17 | 126 \pm 6 | 66\pm3 | |
| EQHD-14 SG | EQ5-U3 | 3a | T-EQH5 | 4.0 | 26.9 | 0.55 | 2.1 | 9.3 | 10 | 671 | 622 | 129 | 1433 \pm 38 | 19/19 59/140 | 17 34 | 104 \pm 4 94 \pm 3 | 72 \pm 4 66\pm3 | |
| EQHD-15 | EQ5-U2 | 2 | T-EQH5 | 4.5 | 26.6 | 0.55 | 2.3 | 8.8 | 10 | 682 | 621 | 122 | 1435 \pm 41 | 20/20 | 8 | 110 \pm 3 | 76\pm3 | |
| EQHD-16 SG | EQ5-U1 | 1 | T-EQH5 | 5.4 | 28.1 | 0.60 | 3.2 | 9.4 | 12 | 801 | 724 | 111 | 1648 \pm 49 | 21/23 3/4 42% | 34 40 | 112 \pm 5 117 \pm 5 | 68 \pm 4 71\pm4 | |
| EQHD-40 | QY-3a | 3a | F | 4.5 | 27.2 | 0.62 | 2.3 | 9.9 | 10 | 730 | 668 | 122 | 1531 \pm 49 | 17/17 | 10 | 95 \pm 3 | 62\pm3 | 2.9 |
| EQHD-41 | QY-3b | 3b | F | 3.9 | 25.3 | 0.65 | 2.7 | 11.0 | 12 | 820 | 761 | 131 | 1724 \pm 56 | 17/17 | 14 | 102 \pm 4 | 59\pm3 | 1.0 |
| EQHD-42 | QY-4 | 4 | F | 3.6 | 25 | 1.16 | 2.6 | 14.0 | 13 | 1144 | 962 | 135 | 2255 \pm 55 | 16/17 | 11 | 101 \pm 3 | 45\pm2 | 0.3 |

| Lab code | Field number | Layer | Area | Depth (m) | Water content (%) | K (%) | U (ppm) | Th (ppm) | Ext. α ($\mu\text{Gy/a}$) | Ext. β ($\mu\text{Gy/a}$) | Ext. γ ($\mu\text{Gy/a}$) | Cosmic ($\mu\text{Gy/a}$) | Total dose ($\mu\text{Gy/a}$) | No. aliquots | OD (%) | D_e (Gy) | CAM Age (Ka) | CaCO_3 (%) |
|---------------|--------------|-------|------|-----------|-------------------|-------|---------|----------|------------------------------------|-----------------------------------|------------------------------------|-----------------------------|---------------------------------|------------------|----------|---------------------------|--|---------------------|
| EQHD-43 | QY-5a | 5a | F | 2.4 | 24.7 | 0.60 | 2.0 | 10.1 | 10 | 713 | 662 | 156 | 1540 \pm 39 | 17/17 | 18 | 103 \pm 5 | 67\pm4 | 2.1 |
| EQHD-44 | QY-5b | 5b | F | 1.9 | 24.6 | 0.35 | 1.35 | 5.6 | 6 | 429 | 392 | 166 | 993 \pm 23 | 16/17 | 26 | 83 \pm 5 | 83\pm5 | 43.8 |
| EQHD-45 | QY-6 | 6 | F | 1.4 | 15 | 0.56 | 1.6 | 7.9 | 9 | 675 | 592 | 176 | 1452 \pm 58 | 17/17 | 39 | 14 \pm 1 | 9\pm1 | 21.3 |
| EQHD-46 | QY-15 | 4 | E | 3.4 | 25 | 0.65 | 0.7 | 3.8 | 4 | 492 | 325 | 139 | 959 \pm 25 | 15/17 | 40 | 105 \pm 5 | 109\pm6 | 4.1 |
| EQHD-47 | QY-16 | 5a | E | 2.3 | 24.6 | 0.62 | 1.9 | 8.9 | 9 | 692 | 614 | 158 | 1473 \pm 47 | 17/17 | 25 | 124 \pm 8 | 84\pm6 | 0.6 |
| EQHD-48 | QY-17 | 3a | E | 4.1 | 22.2 | 0.60 | 1.9 | 10.0 | 10 | 716 | 663 | 128 | 1516 \pm 54 | 17/17 | 11 | 113 \pm 4 | 74\pm4 | |
| EQHD-49 | QY-18 | 3b | B | 3.6 | 22.3 | 0.66 | 1.9 | 10.8 | 10 | 764 | 704 | 135 | 1614 \pm 41 | 17/17 | 15 | 105 \pm 4 | 65\pm3 | 2.1 |
| EQHD-50 SG | QY-19 | 3a | B | 3.9 | 14.8 | 0.42 | 1.6 | 6.7 | 8 | 567 | 509 | 131 | 1209 \pm 26 | 17/17 2/3 57% | 13 30 | 116 \pm 4 85 \pm 2 | 96 \pm 4 71\pm3 | 38.6 |
| EQHD-51 | QY-20 | 3a | B | 4.2 | 26.9 | 0.59 | 2.3 | 11.6 | 11 | 753 | 731 | 127 | 1621 \pm 54 | 17/17 | 10 | 113 \pm 3 | 70\pm3 | 2.2 |
| EQHD-52 | QY-14 | 4a | E | 3.8 | 26.3 | 1.25 | 2.3 | 11.5 | 11 | 1099 | 850 | 132 | 2029 \pm 63 | 17/17 | 11 | 151 \pm 5 | 72\pm3 | 1.0 |

No. aliquots – the number of aliquots used for the average D_e out of those measured. For single grains (SG), this indicates the number of components isolated using the finite mixture model (FMM) (Galbraith & Roberts 2012) and the percentage of the largest component. OD, overdispersion. D_e averages and errors were calculated using the central age model (CAM). Ages of single-grain samples, used in the remainder of the discussion, are in **bold**. Samples highlighted in gray were not used for layer averages.

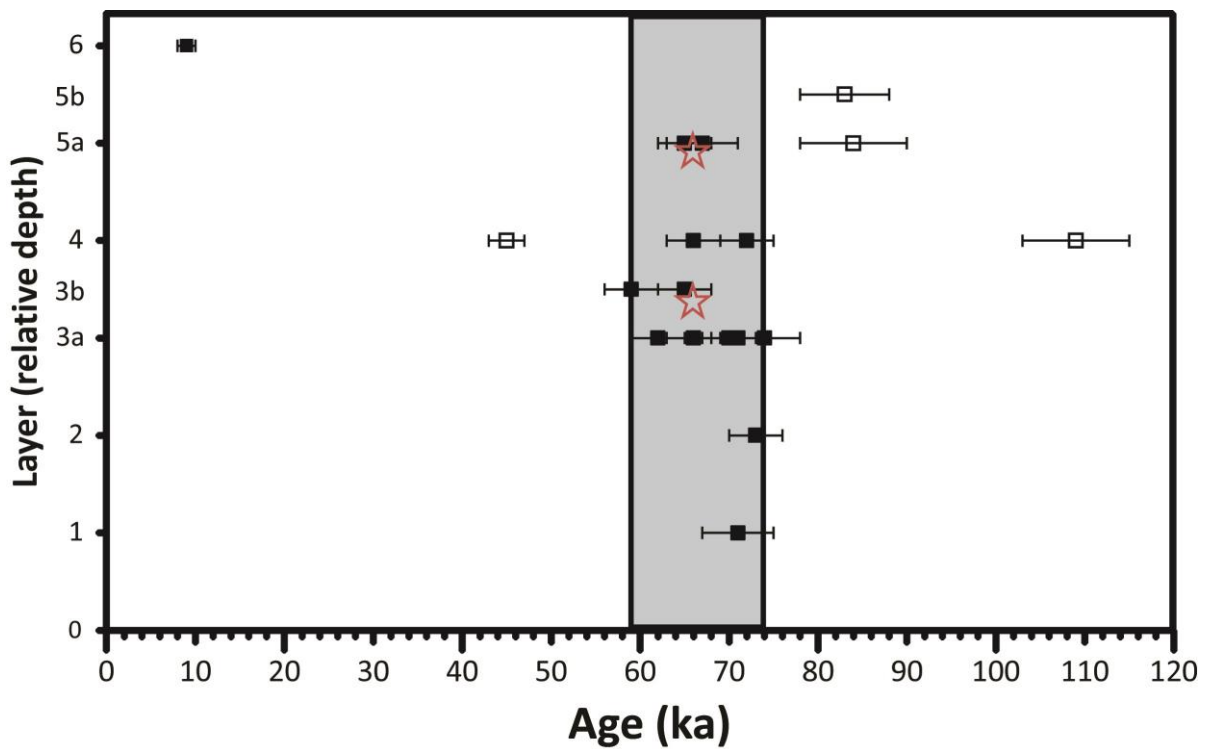
SI 2 Table 2. Samples that were not in stratigraphic order and their recalculated ages using a site-averaged dose rate of 1.55 Gy/ka. (See text for details.)

| Sample | D_e (Gy) | Dose rate (Gy/ka) | Age (ka) | Expected Age (ka) | Recalculated Age (ka) | CaCO ₃ (%) |
|---------|---------------|----------------------|-------------|----------------------|--------------------------|--------------------------|
| EQHD-42 | 101 | 2.26 | 45±2 | <~60-65 | 65 | 0.3 |
| EQHD-44 | 85 | 0.99 | 83±5 | <~60-65 | 54 | 43.8 |
| EQHD-46 | 105 | 0.96 | 109±6 | <~70 | 68 | 4.1 |
| EQHD-47 | 124 | 1.47 | 84±6 | <~70 | 80 | 0.6 |

SI 2 Table 3. Averaged ages for each unit. The ages for Layer 3b are shown from above and below the femur; an average for the entire unit is also shown.

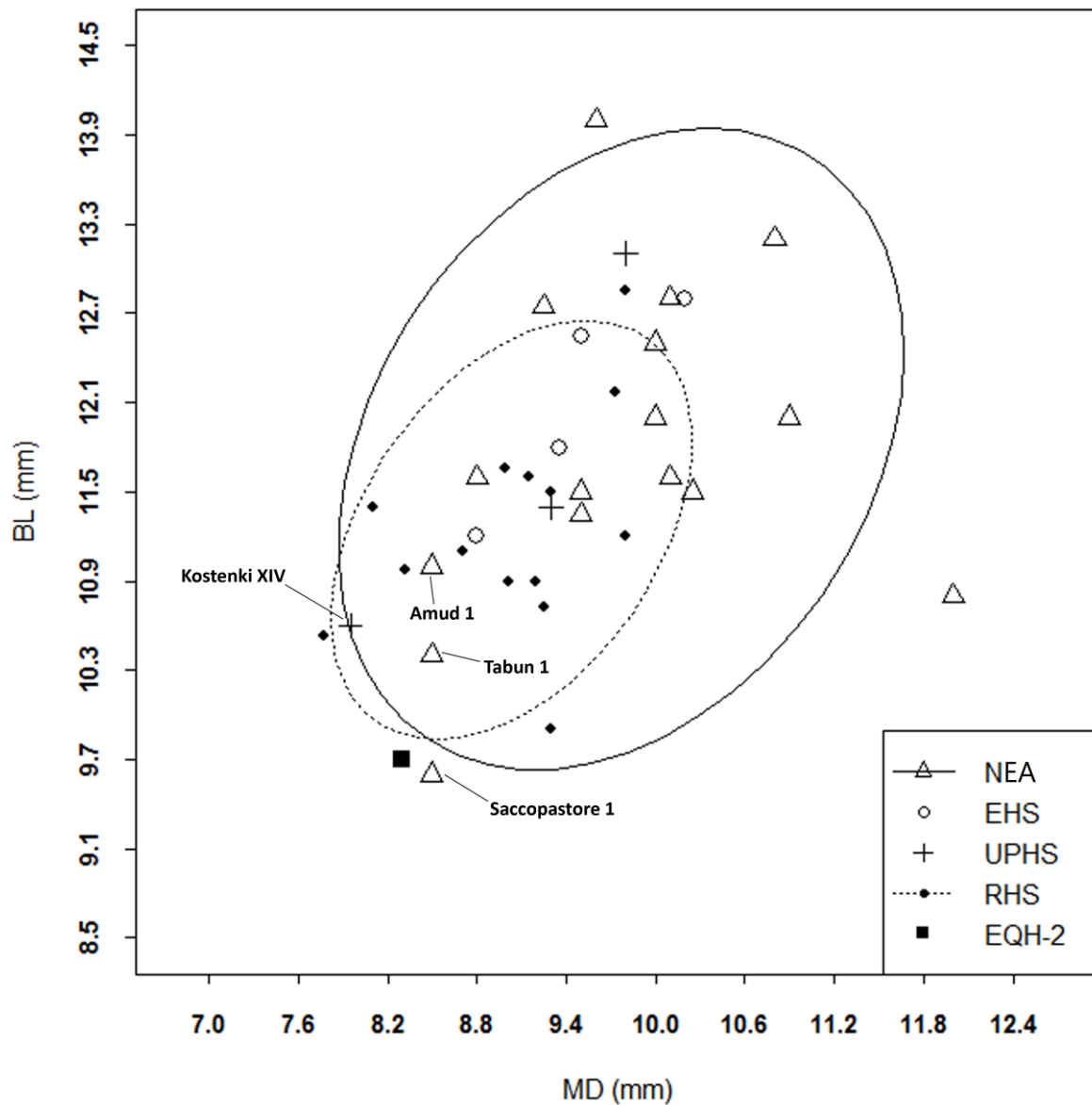
| Layer | Sample lab codes (EQHD) | N | Average (ka) |
|------------------|----------------------------|---|-----------------|
| 1 | 16 | 1 | 71±4 |
| 2 | 15 | 1 | 76±3 |
| 3a | 14,40,48,51 | 4 | 68±5 |
| 3b (below femur) | 41,50 | 2 | 65±8 |

| Layer | Sample lab codes (EQHD) | N | Average (ka) |
|------------------|-------------------------|---|--------------|
| 3b (above femur) | 49 | 1 | 65±3 |
| 3b (average) | 41,49,50 | 3 | 65±6 |
| 4, 4a | 13, 52 | 2 | 69±3 |
| 5a | 12,43 | 2 | 66±1 |
| 5b | 44 | 1 | 54±5* |
| 6 | 45 | 1 | 9±1 |

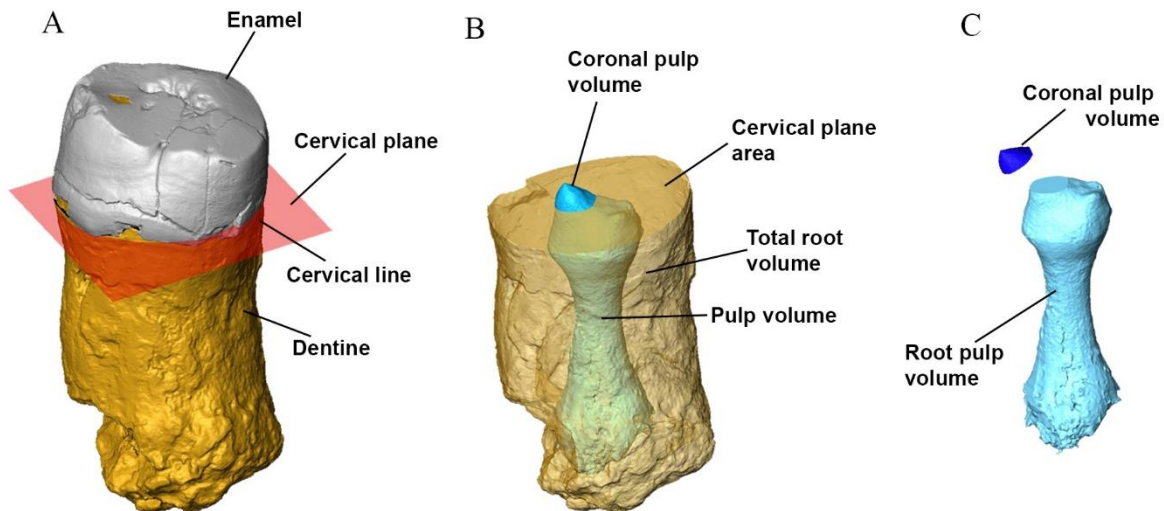


SI 2 Fig. 1. Ages of the stratigraphic layers (black rectangles) with their associated errors (bars). Red stars indicate human remains. Open squares indicate the outliers.

SI 3. EQH-2 (Upper Third Molar)



SI 3 Fig.1. Scatterplot of MD diameter vs. BL diameter of M³. NEA, Neandertal; EHS, early *H. sapiens*; UPHS, Upper Palaeolithic *H. sapiens*; RHS, recent *H. sapiens*. In the scatterplot, the 95% confidence ellipses are reported for NEA and RHS.



SI 3 Fig. 2. Root metric analysis. (A) The root of EQH-2 (RM³) was separated from the crown along the best-fit plane computed at the cervical line (cervical plane). (B) The root was separated in two parts: total root volume and pulp volume. (C) The pulp volume was divided by the cervical plane into coronal pulp volume and root pulp volume.

SI 3 Table 1. Nonmetric dental traits observed in the enamel-dentine junction of EQH-2 (RM³) vs. the frequency of these traits (%) in Neandertals (NEA), early and Upper Palaeolithic *H. sapiens* (EHS and UPHS), and recent *H. sapiens* (RHS).

| Specimen/Taxon | <i>n</i> | Hypocone | Carabelli's trait | Distal accessory tubercle | Mesial accessory tubercle | Paracone accessory cusp |
|----------------|----------|----------|-------------------|---------------------------|---------------------------|-------------------------|
| EQH-2 | 1 | Absent | Absent | Absent | Present | Present |
| NEA | 16 | 100 | 56.6 | 31.25 | 50 | 100 |
| EHS and UPHS | 12 | 83.3 | 41.5 | 16.6 | 50 | 41.6 |
| RHS | 18 | 83.3 | 61.1 | 11.1 | 11.1 | 38.8 |

SI 3 Table 2. Dental crown diameters (MD and BL), in mm, of M³ in EQH-2 and the comparative sample.

| Specimen/Taxon | <i>n</i> | MD | | | | BL | | | |
|----------------|----------|------|------|------|------|-------|------|------|-------|
| | | Mean | SD | Min. | Max. | Mean | SD | Min. | Max. |
| EQH-2 | 1 | 8.3 | | | | 9.7 | | | |
| NEA | 16 | 9.76 | 0.96 | 8.5 | 12 | 11.78 | 1.10 | 9.6 | 13.2 |
| EHS | 4 | 9.46 | 0.57 | 8.8 | 10.2 | 12.08 | 0.72 | 11.2 | 12.8 |
| UPHS | 3 | 9.01 | 0.95 | 7.95 | 9.8 | 11.7 | 1.27 | 10.6 | 13.1 |
| RHS | 14 | 9.03 | 0.61 | 7.77 | 9.8 | 11.24 | 0.71 | 9.9 | 12.85 |

NEA, Neandertal; EHS, early *H. sapiens*; UPHS, Upper Palaeolithic *H. sapiens*; RHS, recent *H. sapiens*.

Neandertals: Jersey 1, La Quina 5, Le Moustier 1, Saccopastore 2, Spy 1, Spy 2, Tabun 1, Vergisson 1, Vergisson 2, La Croze del Dua 3, La Croze del Dua 4 (76), Amud 1 (77), Shanidar 1, Shanidar 2, Shanidar 4 (33), Krapina 58 (78). EHS: Skhul 4, Skhul 5, Skhul 7 (76), Qafzeh 9 (79). UPHS: Dolni Věstonice 3 (76), Kostenki XIV, Sungir 2 (provided by Bence Viola, Institute of Anthropology, Russian Academy of Sciences, Saint Petersburg). RHS: Vasilyevka III-55 Sloi IV 12, Vasilyevka III-55 N 33, NHMW Breitinger Nr. 87, NHMW Breitinger Nr. 85, NHMW 811, NHMW 9687, Bruckneudorf G905/1, Bruckneudorf G899, NHMW 6034, Bystrovka 3 K7 N 30, NHMW 6031, NHMW 15358, NHMW 15357, Ushauz Cave Sk 1 (provided by Bence Viola, Institute of Anthropology, Russian Academy of Sciences, Saint Petersburg).

SI 3 Table 3. List of fossil and extant human upper third molars (M3) used for enamel thickness and root analysis.

| Taxon | Specimen | Wear stage ¹ | Enamel thickness | Root |
|-------|-----------------|-------------------------|------------------|------|
| NEA | BD8 | 2 | X | |
| | El Sidron SD332 | 2 | X | |
| | El Sidron SD621 | 1 | X | X |
| | El Sidron SD741 | 2 | X | |
| | Kebara KMH24 | 2 | X | |
| | Krp D162 | 3 | X | X |
| | Krp D163 | 2 | X | X |
| | Krp D170 | 2 | X | |
| | Krp D173 | 3 | | X |

| Taxon | Specimen | Wear stage ¹ | Enamel thickness | Root |
|-------|-------------------|-------------------------|------------------|------|
| | Krp D178 | 2 | X | X |
| | Krp D180 | 2 | X | |
| | Krp D58 | 2 | X | X |
| | Krp D99 | 2 | X | |
| | Le Moustier 1 | 1 | X | |
| | Marillac | 1 | X | X |
| | St-Cesaire | 2 | X | X |
| EHS | Qafzeh 11 | 1 | X | |
| | Qafzeh 26 | 2 | X | X |
| | Skhul 4 | 4 | X | |
| UPHS | Combe Capelle | 2 | X | X |
| | Equus Cave EQ-H12 | 4 | X | X |
| | Hayonim 19 | 1 | X | |
| | Hayonim 25 | 3 | X | X |
| | Hayonim 8 | 3 | X | X |
| | Les Rois | 4 | | X |
| | Nahal Oren 24 | 1 | X | X |
| | Nahal Oren 16 | 2 | | X |
| | Oberkassel D999 | 2 | X | X |
| | Ohalo H2 | 2 | X | |
| | Villabruna 1 | 1 | X | X |
| RHS | 565 | 2 | X | X |
| | FJRI r2064-1420 | 1 | X | |
| | FJRI r2643-1941 | 1 | X | |
| | FJRI r605-1185 | 2 | X | X |
| | M072 | 2 | X | X |
| | M091 | 2 | X | X |
| | M152 | 2 | X | X |
| | M157 | 2 | X | X |
| | M160 | 2 | X | |
| | M194 30 | 2 | X | X |
| | M197 | 2 | X | X |
| | M199 | 2 | X | X |

| Taxon | Specimen | Wear stage ¹ | Enamel thickness | Root |
|-------|----------------------|-------------------------|------------------|------|
| | M20 | 2 | X | X |
| | M246 | 2 | X | X |
| | M249 | 2 | X | X |
| | M65 0385 | 2 | X | X |
| | Ulac 536 | 2 | X | X |
| | Wittenberg 2192-39-a | 2 | X | X |

NEA, Neandertal; EHS, early *H. sapiens*; UPHS, Upper Palaeolithic *H. sapiens*; RHS, recent *H. sapiens*.

¹Based on Molnar (30).

SI 3 Table 4. Three-dimensional enamel thickness of EQH-2 (RM³) standardized to z scores (for RET index) of the *H. heidelbergensis* (HH), Neandertal (NEA), early and Upper Palaeolithic *H. sapiens* (EHS and UPHS), and recent *H. sapiens* (RHS) M³ sample for different wear stages. (Standard deviation is indicated in brackets.)

| Specimen/Taxon | Wear stage ¹ | <i>n</i> | AET (mm) | | RET (scale free) | | z scores for RET index |
|----------------|-------------------------|----------|-------------|-----------|------------------|-------------|------------------------|
| | | | Mean | Range | Mean | Range | |
| EQH-2 | 3 | | 0.95 | | 18.9 | | |
| HH | 2 | 1 | 1.2 | | 23.5 | | |
| NEA | 1–3 | 16 | 1.22 (0.13) | 0.95–1.45 | 19.66 (2.25) | 15.42–28.36 | -0.33 |
| EHS and UPHS | 1–3 | 10 | 1.39 (0.17) | 1.05–1.58 | 25.01 (3.85) | 19.42–32.37 | -1.58 |
| EHS and UPHS | 4 | 2 | 0.88 (0.02) | 0.87–0.90 | 15.49 (1.28) | 14.58–16.40 | 1.01 |
| RHS | 1/2 | 18 | 1.45 (0.14) | 1.23–1.70 | 26.48 (4.20) | 20.19–35.92 | 1.81 |

AET, average enamel thickness index; RET, relative enamel thickness index.

¹Based on Molnar (30).

SI 3 Table 5. Three-dimensional root analysis of EQH-2 (RM³) standardized to z scores of the *H. heidelbergensis* (HH), Neandertal (NEA), early *H. sapiens* (EHS), Upper Palaeolithic *H. sapiens* (UPHS), and recent *H. sapiens* (RHS) M³ sample.

| Specimen/ | | | | | | | | | | | | | |
|-----------|----------|-----------------|----------|--------------------|----------|------------------|----------|----------------|----------|------------------|----------|------------------|----------|
| Taxon | <i>n</i> | R.L. | | T.R.V. | | P.V. | | C.P.V. | | R.P.V. | | C.P.A. | |
| | | Mean | <i>z</i> | Mean | <i>z</i> | Mean | <i>z</i> | Mean | <i>z</i> | Mean | <i>z</i> | Mean | <i>z</i> |
| | | (SD) | score | (SD) | score | (SD) | score | (SD) | score | (SD) | score | (SD) | score |
| EQH-2 | 1 | 14.24 | | 600.14 | | 73.39 | | 1.00 | | 72.38 | | 55.27 | |
| HH | 1 | 13.12 | | 388.93 | | 30.75 | | 2.64 | | 28.11 | | 52.74 | |
| NEA | 7 | 15.77 (1.90) | 0.80 | 728.61 (200.06) | 0.64 | 65.89 (27.25) | 0.27 | 3.36 (3.43) | 0.68 | 62.62 (28.74) | 0.33 | 80.34 (7.42) | 3.37 |
| EHS | 1 | 14.20 | | 483.34 | | 57.25 | | 2.09 | | 55.15 | | 67.40 | |
| UPHS | 9 | 12.89 (1.63) | 0.82 | 381.45 (78.18) | 2.79 | 27.82 (8.073) | 5.64 | 3.13 (4.72) | 0.33 | 24.68 (5.70) | 8.36 | 66.48 (7.14) | 1.57 |
| RHS | 15 | 11.44 (1.73) | 1.62 | 393.57 (111.73) | 1.84 | 38.15 (17.26) | 2.04 | 4.64 (5.34) | 0.68 | 32.63 (13.96) | 2.84 | 60.85 (11.42) | 0.48 |

R.L., root length; T.R.V., total root volume; P.V., pulp volume; C.P.V., coronal pulp volume; R.P.V., root pulp volume; C.P.A., cervical plane area.

SI 4. Description of the EQH-3 Bones

The EQH-3 specimen consists of five lower limb bones: left femur, right and left tibia, and right and left fibulae. Only the femur and tibiae are the subject of this research.

The femur (Figure 4)

Nearly complete from the articular condyles up to the head, the femur is eroded at the epiphyses and fragmented at the diaphysis. It is robust and highly curved in the sagittal plane, with the apex of the curvature distal to the midshaft. The bicondylar length of the femur is 438 mm and its biomechanical length is 407 mm, both within the range reported for *H. sapiens* and slightly higher than the mean for Neandertals. Note that the bicondylar length might have been slightly longer if the bone were complete (SI 4 Tables 1 and 3). Broken parts of the bone were reconstructed by Yoel Rak.

The proximal femur: The femoral head is partially broken and eroded. The neck is eroded, and its remaining part is distorted, probably due to taphonomic changes. There are remains of the greater and lesser trochanters, but they do not suffice for a full description. The neck shaft angle (119°) indicates coxa vara. The angle of torsion (19°) indicates a high degree of anteversion (SI 4 Tables 1 and 3).

The femoral shaft: The shaft is complete but fragmented. Its overall shape is robust and highly curved, with a smooth anterior surface, while the posterior surface is roughened by the linea aspera. The femoral pilaster (linea aspera pilaster) on the posterior surface of the shaft is missing. The popliteal surface on the posteroinferior part of the femoral shaft is flat and mediolaterally broad. The midshaft shape ratio (with a pilastric index of 99.1) indicates a rounded cross section (the anteroposterior diameter and the mediolateral diameter are nearly equal). The midshaft robusticity index (14.9) is very high in comparison with that of *H. sapiens* (early and recent) and Neandertals, indicating a very robust femur (SI 4 Table 3). The

subpilastric index of the femur (85.6%) reflects the widening of the femoral shaft toward its distal end (at 25% of the femur length).

The distal femur: Both the medial and the lateral condyles of the femur are preserved, but the medial condyle is eroded on its medial side. The medial articular surface is nearly complete; its surface is smooth and wide. The medial epicondyle is eroded, but the adductor tubercle projects medially from the proximal end of the medial condyle. The lateral condyle is longer (along the anteroposterior axis) and narrower (along the mediolateral axis) than the medial condyle. A shallow pit (3 cm in diameter) can be seen on the lateral surface of the lateral condyle, probably due to postmortem pressure exerted on the bone. The intercondylar fossa, located between the two distal articular condyles, is extremely narrow. Its unique shape is not usually seen in the distal femora of *H. sapiens* or Neandertals. The maximum mediolateral condylar breadth and the epiphyseal breadth ratio are small compared with those of Neandertals and *H. sapiens* (SI 4 Tables 1 and 3). This is the result of the narrow lateral condyle and the very narrow intercondylar notch.

Computed tomography (CT) scanning of the bone reveals that the total cross-sectional area of the midshaft is large and the cortical bone is relatively thick (SI 4 Table 3). The CT scan also shows the presence of an epiphyseal line at the distal femur, in accordance with ossification stage 3 out of 4, where the fourth stage implies full ossification (41, 42).

The right tibia (Fig. 4F)

The right tibia is missing its proximal part: the remains include the diaphysis, distal to the soleal line, and the distal epiphyses. The proximal end of the tibial shaft is eroded, and the shaft itself is fragmented and slightly distorted. The anterior crest of the tibial shaft is rounded. The interosseous border is smooth and rounded, resulting in a continuation between the posterior, the medial, and the lateral surface of the tibial shaft. The medial surface of the tibia is wide, with a fracture line running along its long axis. Just proximal to the talar facet is

a marked groove running from the medial to the lateral surface, on the anterior side. This groove was caused by tools used in the excavation.

The distal end of the right tibia is remarkably complete. The fibular notch, on its lateral side, is flat and wide. The talar facet has a trapezoid shape; its lateral side is wider than its medial one. The prominent medial malleolus is nearly complete. A squatting facet is seen on the anteroinferior edge of the tibia (SI 4 Tables 2 and 4).

The left tibia (Fig. 4E):

The left tibia is nearly complete; it extends from the tibial plateau to the talar facet, but it is missing the medial malleolus. The tibial plateau is flat, and its peripheral edges are eroded. A robust intercondylar tubercle (the medial part of the intercondylar eminence) is clearly visible between the two condyles. The lateral part of the intercondylar eminence is missing. Three centimeters distal to the tibial plateau, on the anterior surface, there is a prominent tibial tuberosity. The superior fibular articular facet is clearly visible on the posterolateral side of the lateral condyle. When viewed laterally, the shaft of the left tibia is fragmented and slightly curved. The shaft is noticeably flattened mediolaterally (i.e., platycnemic). As in the right tibia, the anterior crest of the tibial shaft is rounded, and the interosseous border is smooth and rounded, forming a continuation between the posterior and the lateral surface of the tibial shaft. (Similar morphology is seen in the tibiae of Palomas 96, Shanidar 1, and Shanidar 2 (80)). The medial surface of the EQH-3 tibia is wide, with a fracture line running along the middle of the surface from the proximal to the distal end. Between the proximal and middle thirds of the posterior surface, the soleal line can be seen (SI 4 Tables 2 and 4).

CT scanning of the tibiae reveals the presence of an epiphyseal line at the proximal and distal tibia. This implies ossification stage 3 out of 4 (where stage 4 indicates complete ossification) (41, 42).

Discussion

Neandertal vs. early *H. sapiens*

We attributed EQH-3 to a Neandertal on the basis of femoral and tibial characteristics. Two hominin species are known to have lived in the area (northern Israel) at the MP: early *H. sapiens* and Neandertals. It has been well established that the Neandertal femora have a suite of characteristic features that include a thick, rounded shaft with a very little or no femoral pilaster, a small angle between the neck and the shaft (coxa vara), and a highly robust femoral shaft (31–34). Researchers have also recently emphasized the high curvature of the femoral shaft of Neandertals as compared to that of *H. sapiens*, and the high cortical bone percentage in the femoral midshaft (35, 36, 81). A number of reasons were suggested for this characteristic morphology, including elevated activity level, adaptation to cold, and locomotion (58, 82–84). The characteristic features documented for the femora of early *H. sapiens* include a gracile and straight femoral shaft, with a small articulation area relative to shaft length. The neck shaft angle is high (coxa valga) (21, 36, 79). The midshaft shows a drop-like cross section (long anteroposterior diameter and short mediolateral diameter), with a well-defined femoral pilaster.

The EQH-3 femur is very robust, and the midshaft robusticity index (14.9) is much higher than that of *H. sapiens* (early and recent) and Neandertals; the index is similar to that of the highly robust femora from Shanidar (33). The midshaft cross section (pilastric index, 99.1%) is rounded (the anteroposterior diameter and the mediolateral diameter are nearly equal), a well-documented Neandertal characteristic that contrasts with the more oval shape of the midshaft in *H. sapiens*, due to a more elongated anteroposterior diameter in *H. sapiens* (33, 36). The femoral shaft of EQH-3 lacks a pilaster and shows a high degree of curvature; both are well-documented Neandertal features. The neck shaft angle (119°, coxa vara) is close to the Neandertal mean and smaller than in *H. sapiens* (124°–130°). The midshaft cross

section of EQH-3 reveals a large cross-sectional area with a relatively high percentage of cortical bone. All of the above characteristics suggest that the femur of EQH-3 belonged to a Neandertal rather than to early or recent *H. sapiens*. It should be noted, however, that Neandertals are characterized by a large articular area in relation to femur length, while in *H. sapiens*, the articular area is smaller (84). The relatively small articular area of the EQH-3 femur (epiphyseal breadth ratio = 16.9) is at the lower end known for Neandertals (16.8 for Tabun C1) and below the Neandertal mean (18.9 ± 1.4) (21, 36). The epiphyseal breadth ratio of EQH-3 is close to that of *H. sapiens* (17.1 ± 1.2).

The Neandertal tibia is robust and characterized by an almond-shape cross section with a relatively rounded anterior crest, almost no prominence of the lateral interosseus crest, and a rounded posterior margin (38). The tibia thus contrasts with the more gracile tibiae of early and recent *H. sapiens*, and their generally angular anterior and interosseous crests (38, 86). The Neandertal tibial diaphysis has been described (33, 86, 87) as mesocnemic or euricnemic (average or wide mediolaterally) while that of *H. sapiens* has been described as platycnemic (narrow mediolaterally), mesocnemic, or euricnemic. It is worth noting that the tibia of early *H. sapiens* is very wide mediolaterally. The tibial tuberosity of Neandertals projects more anteriorly than in *H. sapiens*, and the tibial condyles are in a posterior position. The tibiae of EQH-3 are morphologically similar to Neandertal tibiae in the former's distinctive, rounded anterior crest and interosseous crest. The robusticity index of the EQH-3 tibia is higher than that of *H. sapiens* and similar to that of Neandertals (SI 4 Table 4). However, the tibial diaphysis is mediolaterally narrow (platycnemic) in comparison to its anteroposterior length, a feature known to occur in recent *H. sapiens* and not common in Neandertals or in early *H. sapiens*. It is worth noting that the tibia of another Neandertal from Israel, Amud 1, is also platycnemic, with a cnemic index of 16.5, similar to that of EQH-3.

The crural index in Neandertals is smaller than that of *H. sapiens*, indicating that the distal segment (tibia) is short in relation to the proximal segment (femur). The crural index of

EQH-3 is lower than the *H. sapiens* mean and higher than the Neandertal mean. The combination of the femoral and tibial features, together with the low crural index, indicates that the bones belonged to a Neandertal.

Age estimation

We used three long-bone indicators to estimate the age of EQH-3: stage of epiphyseal union, bone length, and age-related pathology (osteoarthritis).

Stage of epiphyseal union: We used the five stages of epiphyseal union described by O'Connor (41) for long bones: non-union (0); beginning union (1), when the epiphyseal and diaphyseal surfaces closely approximate each other; active union (2), when the epiphysis and diaphysis cap each other; recent union (3), when the epiphysis and diaphysis have united to form a single unit of bone, the position of the former epiphysis and diaphysis can still be distinguished, and a fine line of fusion of greater density may remain between the epiphysis and diaphysis; and complete union (4), when the epiphysis and diaphysis are united as a single unit of bone. The distal epiphysis of the femur of EQH-3 and the proximal and distal epiphysis of the tibiae can be assigned to stage 3. A fine line of fusion of greater density (epiphyseal line) is clearly visible in the CT scan between the epiphysis and diaphysis. Stage 3 can be seen in young adults between the ages of 15 and 22 in modern human populations.

Long bone length: We compared the length of the bones of EQH-3 to the femoral and tibial lengths of other Neandertals. The comparison indicates that the long bones of EQH-3 reached full or nearly full adult length.

Age-related pathology: No age-related pathology was identified on any of the bones. We can conclude from these three indicators that the bones of EQH-3 belonged to a young adult (15–22 y) (41, 42).

Male vs. female

The pattern of sexual dimorphism in European and Near Eastern Neandertals is virtually indistinguishable from that of recent *H. sapiens*. Male and female Neandertals are distinguished by their limb bone lengths and articular dimensions. The degrees of size dimorphism found in single-site samples and in the total sexable Neandertal sample are within the expected ranges of variation for the recent *H. sapiens* samples. Furthermore, no differences exist between the Neandertal and recent *H. sapiens* samples with respect to postcranial robusticity as an indicator of sexual dimorphism. In both the fossil and recent samples, the males tend to be slightly more robust than the females, and there is extensive overlap between the sexes (69).

In terms of length and robusticity, the femur of EQH-3 falls within or above the mean for Neandertal males. The tibia presents a somewhat more complex picture. The tibial length falls above the mean for Neandertal males and significantly above the length of Neandertal females. Tibial robusticity, however, falls closer to the mean for Neandertal females than Neandertal males (SI 4 Table 5). Neandertal males also show a lower cnemic index than Neandertal females (SI 4 Table 5); the platycnemic tibia of EQH-3 is at the lower range known for Neandertal males (similar to that of Amud 1) and significantly below the range for Neandertal females (33, 69).

We conclude from this analysis that the bones of EQH-3 belonged to a Neandertal male.

Estimated stature

Stature estimation is used in the reconstruction of the individual's physique during life and provides an indication of size and body mass (40). In fossil hominins, stature is estimated using correlations from recent *H. sapiens* populations. Many formulas for using long bones to calculate stature are found in the literature (88-91, to name a few). We used three types of formulas: formulas based on femur length, formulas based on tibial length, and formulas based on femoral and tibial length (SI 4 Table 6). Using these formulas, we estimated the

stature of EQH-3 to be between 159.9 and 168.6 cm, and we estimated the mean calculated height of EQH-3 to be 163.6 cm (SI 4 Table 6).

The stature of EQH-3 is within the normal range for modern humans, and the specimen would be classified as being of below medium height. The height of EQH-3 is significantly below the estimated height for early *H. sapiens* (males and females), close to the mean for Neandertal males, and above the mean for Neandertal females. A comparison with the hominin specimens from Sima de los Huesos shows that the stature of EQH-3 falls right in the middle between the males and the females (40) (SI 4 Table 7).

Discrepancy between shaft robustness and small articular area

The surprising combination of the very robust diaphysis and the slender epiphysis in the femur of EQH-3 gives rise to some intriguing hypotheses.

The morphology of articular surfaces reflects their weight-bearing properties as well as the stability and mobility of the joints to which they contribute. Osteogenic responses to mechanical loading are known for compact bone in the diaphysis cross section and for trabecular bone in the epiphysis (92). Lieberman (92) claims that the articular surface area is ontogenetically constrained and related to locomotor behavior at the species level and to body mass at the individual level. At the same time, diaphysis cross-sectional geometry is related to individual variations in activity level. This would suggest that EQH-3 was relatively lightweight or avoided bearing weight on his left knee while still maintaining a high activity level.

Knee pathology

The distal femur and proximal adjacent tibia (left) exhibit some morphological peculiarities. These include the very narrow intercondylar notch, the small lateral articular facet of the distal femur, and the prominent tibial intercondylar eminence between the two

tibial plateaus. These features are different from the femur and tibia of Neandertals and *H. sapiens* (SI 4 Tables 3 and 4). In an attempt to understand the nature of these features, we tested three hypotheses:

(1) This is a plesiomorphic characteristic that can be found in the femur or tibia of other hominins.

(2) This morphology is the result of taphonomy.

(3) The combination of these morphologies represents knee pathology.

After examining the literature and casts of the distal femur and proximal tibia of both *H. erectus* specimens and australopithecines, we concluded that the unique morphology of the knee joint of EQH-3 is different from the morphology of the knee joints of *H. erectus* and australopithecine specimens. We therefore rejected our first hypothesis.

The narrow intercondylar notch might indeed be a result of taphonomical changes, but these cannot be the cause of the small articular condyles and the protruding intercondylar eminence. We therefore partially rejected our second hypothesis.

The medial intercondylar eminence is the attachment area for the anterior cruciate ligament (ACL), one of the four major ligaments that stabilize the knee joint (93). This ligament prevents the knee from going into hyperextension. A narrow intercondylar notch together with a very prominent intercondylar eminence is associated with a well-known knee pathology—a bony avulsion of the ACL (94–96). These injuries occur most commonly in skeletally immature individuals between the ages of 8 and 14 (43). The mechanism for ACL tearing with or without avulsion is usually traumatic: an unexpected knee hyperextension or a blow to the lateral side of the knee. Patients with ACL avulsion fractures will develop knee hemarthrosis within 12–16 hours, and an inability to walk and run in the days or weeks after the injury. In order to survive, EQH-3 would have had to rely on help from members of his group shortly after the injury occurred. After the acute stage is over, in the months and years after the injury, individuals with ACL avulsion fractures can walk and run but might suffer

from knee instability when trying to bear weight (94, 96). If such a pathology did occur in the knee of EQH-3, he might have suffered from instability of the left knee joint and thus tried to bear less weight on his left leg than on his right leg. The small articular surface of the distal femur might be the result of that pathology, as articular surface area is directly related to the amount of axial pressure exerted on the joint. We therefore determined that the third hypothesis is most likely the correct one.

SI 4 Table 1. Description of femur measurements. The numbering of the measurements corresponds to the numbers in SI 4 Fig. 1; note that the measurements in brackets are not depicted in the figure. Unless otherwise specified, measurements are in millimeters.

| Measurement | Description |
|--|---|
| 1. Femur bicondylar length (Martin* #2) | Maximum length between the femoral head and the distal condyles |
| 2. Femur biomechanical length | The distance between the most inferior point of the superior femoral neck and the distal condyles |
| 3. Neck shaft angle (degrees) (Martin #29) | The angle between the shaft and the neck |
| [4. Torsion angle (degrees) (Martin #28)] | The angle between the axis of the femoral neck and the tangent of the posterior surface of the femoral condyles |
| [5. Femoral AP midshaft diameter (Martin #6)] | The anteroposterior length of the femoral midshaft |
| 6. Femoral ML midshaft diameter (Martin #7) | The mediolateral breadth of the femoral midshaft |
| [7. Midshaft shape ratio (pilastric index)] | (Anteroposterior midshaft diameter/mediolateral midshaft diameter) \times 100 |
| [8. Midshaft circumference (Martin #8)] | The minimum circumference of the femoral midshaft |
| [9. Subpilastric index] | (Anteroposterior diameter/mediolateral diameter) \times 100, at the inferior quarter of the femoral shaft (75% of femur length) |
| [10. Robusticity index [†]] | (Mediolateral midshaft diameter/bicondylar breadth) \times 100 |

| Measurement | Description |
|--|---|
| [11. Robusticity index [‡]] | (Mediolateral midshaft diameter + anteroposterior midshaft diameter) × 100/femur bicondylar length |
| 12. Maximum ML condylar breadth (Martin #21) | The maximum mediolateral breadth of the distal femur |
| 13. ML breadth of lateral condyle | The maximum mediolateral breadth of the lateral condyle |
| [14. AP length of lateral condyle] | The maximum anteroposterior length of the lateral condyle |
| 15. ML breadth of medial condyle | The maximum breadth of the medial condyle |
| 16. AP length of medial condyle | The maximum anteroposterior length of the medial condyle |
| [17. Epiphyseal breadth ratio] | (Maximum condylar breadth/biomechanical length) × 100 |
| 18. Intercondylar fossa breadth | The distance between the medial wall of the lateral condyle and the lateral wall of the medial condyle at the midcondyle anteroposterior length |
| 19. Intercondylar fossa depth | The horizontal distance between the most anterior point of the inferior border of the intercondylar notch and the tangent to the posterior surface of the femoral condyles |
| 20. Chord | In a medial view, the distance between the deepest (most dorsal) point of the anterior femoral contour (just distal to the greater trochanter) and the maximum concavity on the anterior distal shaft (just proximal to the patellar surface) |

| Measurement | Description |
|--|---|
| 21. Subtense (Martin #27) | The perpendicular distance from the chord line to the anterior shaft at maximum curvature |
| 22. Point of maximum curvature | The position of the point of the femur's maximum curvature |
| [23. Total cross-sectional area (mm ²)] | The total cross-sectional area of the midshaft |
| [24. Cortical cross-sectional area (mm ²)] | The cortical area of the midshaft's cross section |
| [25. Cortical area ratio] | $(\text{Cortical area}/\text{total area}) \times 100$ |

*All citations of Martin in this table refer to Martin (68).

†Trinkaus (32)

‡De Groote (36)

SI 4 Table 2: Description of tibia measurements. The numbering of the measurements corresponds to the numbers in SI 4 Fig. 2; note that the measurements in brackets are not depicted in the figure. Unless otherwise specified, measurements are in millimeters

| Measurement | Description |
|-------------------------------|--|
| [1. Actual length] | The distance between the most proximal point and the most distal point of the tibia |
| 2. Tibia biomechanical length | The distance between the talar facet and the articular condyle facet |
| 3. Maximum tibial length | For 'Ein Qashish, a composite consisting of the actual length of the left tibia and the medial malleolus length of the right tibia |

| Measurement | Description |
|--|---|
| 4. Proximal epiphyseal breadth | The distance between the most lateral end and the most medial end of the proximal tibia |
| [5. AP diameter at $\frac{1}{3}$ of total tibial length] | The anteroposterior diameter of the tibial shaft at one-third of its length, at the nutrient foramen |
| [6. Mediolateral diameter at $\frac{1}{3}$ of total tibial length] | The mediolateral diameter of the tibial shaft at $\frac{1}{3}$ of its length |
| [7. Cnemic index at $\frac{1}{3}$ of total tibial length] | (Mediolateral diameter at $\frac{1}{3}$ tibial length/anteroposterior diameter at $\frac{1}{3}$ tibial length) \times 100 |
| [8. Midshaft AP diameter] | The anteroposterior diameter of the tibial shaft at 50% of its length |
| [9. Midshaft ML diameter] | The mediolateral diameter of the tibial shaft at 50% of its length |
| [10. Cnemic index at midshaft] | (Midshaft mediolateral diameter/midshaft anteroposterior diameter) \times 100 |
| [11. Midshaft circumference] | The circumference at the midshaft |
| [12. Robusticity index] | The square root of the product of the anteroposterior diameter and the mediolateral diameter at the midshaft, divided by the maximum tibial length, times 100 |
| 13. Distal tibia maximum ML breadth | The maximum mediolateral breadth of the distal tibia |
| 14. Distal tibia maximum AP length | The maximum anteroposterior length of the distal tibia |
| 15. Distal articular facet maximum ML breadth | The maximum mediolateral breadth of the distal articular facet |

| Measurement | Description |
|--|--|
| 16. Distal articular facet, medial end, maximum AP length | The maximum anteroposterior length of the distal articular facet, at the medial end |
| 17. Distal articular facet, lateral end, maximum AP length | The maximum anteroposterior length of the distal articular facet, at the lateral end |
| 18. Medial malleolus length | The vertical distance between the distal end of the articular facet and the tip of the malleolus |

SI 4 Table 3: Femur measurements of EQH-3, recent *H. sapiens*, early *H. sapiens*, and Neandertals.

| Measurement | EQH-3 | Recent <i>H. sapiens</i> | Early <i>H. sapiens</i> | Neandertals |
|---------------------------------|-------|--|--|---|
| | | $X \pm sd$ | $X \pm sd$ | $X \pm sd$ |
| Femur bicondylar length (mm) | 438 | $443.4 \pm 26.3^*$ (Europeans); $426.5 \pm 34.2^\dagger$ | $492 \pm 20.4^*$ (Skhul hominids); $460.5 \pm 36.7^\ddagger$ $456.1 \pm 34.2^\dagger$ | $430.6 \pm 27.9^*$ $434.8 \pm 26.2^\ddagger$ $430.3 \pm 32.1^\dagger$ |
| Femur biomechanical length (mm) | 407 | N/A | 454.3^\S (Skhul hominids) | 409.6^\S |
| Neck shaft angle (degrees) | 119 | $128.5 \pm 4.7^*$ $127.4 \pm 5.7^\dagger$ | $130 \pm 7.0^*$ $124.3 \pm 7.6^\dagger$ | $120 \pm 5.3^*$ $118.7 \pm 5.2^\dagger$ |
| Torsion angle (degrees) | 19 | $16.7 \pm 6.9^\dagger$ | $11.2 \pm 9.9^\dagger$ | $10.4 \pm 14.9^\dagger$ |

| Measurement | EQH-3 | Recent <i>H. sapiens</i> | Early <i>H. sapiens</i> | Neandertals |
|--|-------|--|--|---|
| | | $X \pm sd$ | $X \pm sd$ | $X \pm sd$ |
| Femoral AP midshaft diameter (mm) | 32.4 | $29.5 \pm 2.8^*$ | $33.8 \pm 3.7^*$ | $29.2 \pm 3.9^*$ |
| Femoral ML midshaft diameter (mm) | 32.7 | $27.6 \pm 2.2^*$ | $27.3 \pm 2.0^*$ | $29.4 \pm 2.1^*$ |
| Midshaft shape ratio (pilastric index) | 99 | 107–119* (range of means of various human populations); $114.2 \pm 19.1^\dagger$ | $120 \pm 14.9^\S$ (Skhul hominids); $128.4 \pm 20.9^\dagger$ $117 \pm 10.4^\parallel$ | 99.3^* $103.0 \pm 14.5^\dagger$ $102 \pm 9.3^\parallel$ |
| Midshaft circumference (mm) | 98.17 | 84.0 ± 4.4 (males) 74.8 ± 4.0 (females) | N/A | 89–108 (Shanidar 4–6) [#] |
| Subpilastric index | 85.6 | $88.1 \pm 15.7^\dagger$ | $102.1 \pm 18.8^\dagger$ | $87.6 \pm 9.8^\dagger$ |
| Robusticity index* | 7.4 | 6.13–6.39* (range of means of various human populations) | 6.19^* | $6.92 \pm 0.16^*$ |
| Robusticity index [†] | 14.9 | $12.4 \pm 1.1^\dagger$ | $13.4 \pm 0.9^\dagger$ | $13.7 \pm 1.0^\dagger$ |
| Maximum ML condylar breadth (mm) | 73.9 | 76.2 ± 2.3 (male) 69.8 ± 2.1 (female) 88.6 ± 4.2 (male) ^{**} 78.5 ± 3.0 (female) ^{**} | 81.6 ± 6.7 (Qafzeh & Skhul hominids) ^{††} | $84.3 \pm 8.0^{\dagger\dagger}$ |

| Measurement | EQH-3 | Recent <i>H. sapiens</i> | Early <i>H. sapiens</i> | Neandertals |
|------------------------------------|-------|---|---|--|
| | | $X \pm sd$ | $X \pm sd$ | $X \pm sd$ |
| ML breadth of lateral condyle (mm) | 22.7 | $25.3 \pm 2.6^{\ddagger\ddagger}$ | N/A | N/A |
| AP length of lateral condyle (mm) | 62.5 | $63.7 \pm 5.1^{\ddagger\ddagger}$ 61.1 ± 3.3 (male)** 55.4 ± 2.1 (female)** | 68.8 ± 5.9 (Skhul hominids) ^{§§} | $66.4 \pm 6.4^{\nabla\ }$ ($N = 7$) |
| ML breadth of medial condyle (mm) | 31.0 | $26.7 \pm 2.7^{\ddagger\ddagger}$ | N/A | N/A |
| AP length of medial condyle (mm) | 61.6 | 61.1 ± 3.4 (male)** 55.9 ± 2.9 (female)** | 61.3 ± 7.2 (Skhul hominids) ^{§§} | $63.3 \pm 8.7^{\nabla\ }$ ($N = 7$) |
| Epiphyseal breadth ratio | 16.9 | $17.1 \pm 1.3^{\dagger}$ | $17.1 \pm 1.2^{\dagger}$ | $18.9 \pm 1.4^{\dagger}$ |
| Intercondylar fossa breadth (mm) | 10.7 | 22 ± 1.8 (male)** 18.7 ± 1.0 (female)** | N/A | N/A |
| Intercondylar fossa depth (mm) | 24.8 | 27.8 ± 1.6 (male)** 23.7 ± 2.0 (female)** | N/A | N/A |
| Chord (mm) | 357 | 254–343 ^{##} (range of means of various human populations) | $334.8 \pm 31.0^{\#\#}$ | $317.6 \pm 28.3^{\#\#}$ |
| Subtense (mm) | 26.6 | 6.2–11.7 ^{##} (range of means of various human populations) | $14.3 \pm 3.0^{\#\#}$ | $15.5 \pm 3.4^{\#\#}$ |
| Point of maximum curvature (mm) | 228 | N/A | $151.2 \pm 21.1^{\#\#}$ | $190.5 \pm 37.0^{\#\#}$ |

| Measurement | EQH-3 | Recent <i>H. sapiens</i> | Early <i>H. sapiens</i> | Neandertals |
|--|-------|--|-----------------------------|-----------------------------|
| | | $X \pm sd$ | $X \pm sd$ | $X \pm sd$ |
| Total cross-sectional area (mm ²) | 749 | 456 ± 62 (African-American females) 440 ± 58 (Caucasian females) | 606.8 ± 95.4 ^{***} | 661.0 ± 54.3 ^{***} |
| Cortical cross-sectional area (mm ²) | 595 | N/A | 459.5 ± 89.3 ^{***} | 523.5 ± 53.6 ^{***} |
| Cortical area percentage | 79.4 | N/A | 75.6 ± 7.3 ^{***} | 79.1 ± 2.7 ^{***} |

*Trinkaus (32)

†De Groote (36)

‡Walker, et al. (80)

§Trinkaus & Ruff (39)

¶Garralda, et al. (97)

#Trinkaus (33)

||Gaikwad & Nikam (98)

**Terzidis, et al. (99)

††Adapted from Vandermeersch (79)

‡‡Ho, et al. (100)

§§Adapted from McCown & Keith (21)

¶¶Adapted from Heim (34)

##Shackelford & Trinkaus (35)

|||Nelson, et al. (101)

***Beauval, et al. (81)

SI 4 Table 4. Tibia measurements of EQH-3, recent *H. sapiens*, early *H. sapiens*, and Neandertals.

| Measurement | EQH-3 | | Recent | Early | Neandertals |
|--|---------------------------|-------------|--------------------------------|---|--|
| | Left tibia | Right tibia | <i>H. sapiens</i> | <i>H. sapiens</i> | |
| Actual length (mm) | 338.5 | 290.7 | N/A | N/A | N/A |
| Tibia biomechanical length (mm) | 332 | N/A | 373 [*] | 409 (Skhul 4); 362 (Cro-Magnon) [*] | 305 (Spy); 298 (Tabun 1) [*] |
| Maximum tibial length (mm) | 338.5 +18.5 = 357.0 | N/A | (349–376) ± 26 [†] | 387 ± 29 [‡] 391 ± 27 [†] | 340 ± 26 [‡] 337 ± 23 [†] |
| Proximal epiphyseal breadth (mm) | 77 | N/A | 70.6 ± 5.5 [§] | N/A | 80 (Shanidar 2) |
| AP diameter at 1/3 of total tibial length (mm) | 38 | N/A | 33.6 ± 4.0 [§] | N/A | 38.4 [‡] |
| ML diameter at 1/3 of total tibial length (mm) | 23 | N/A | 22.6 ± 1.5 [§] | N/A | 26.6 [‡] |

| Measurement | EQH-3 | | Recent <i>H. sapiens</i> | Early <i>H. sapiens</i> | Neandertals |
|--|------------|-------------|--|--|--|
| | Left tibia | Right tibia | | | |
| Cnemic index at 1/3 of total tibial length | 60 | N/A | 64–72 ± 6 [‡] (range of means of various human populations) | 64 ± 6 [‡] | 69 ± 6 [‡] |
| Midshaft AP diameter (mm) | 36.9 | 35.32 | N/A | 35 ± 2.1 [¶] (Skhul & Qafzeh hominids) | 33.1 ± 3.5 [#] |
| Midshaft ML diameter (mm) | 21.5 | 21.21 | N/A | 24.8 ± 1.5 [¶] (Skhul & Qafzeh hominids) | 23.1 ± 2.3 [#] |
| Cnemic index at midshaft | 58 | 60 | 59.6–74.8 [#] (range of means of various human populations) | 78.8 ± 2.3 (Skhul & Qafzeh hominids) [#] | 68.9 ± 6.6 (males) [#] 74.8 ± 0.5 (females) [#] 69 ± 6 [‡] (pooled sample) |

| Measurement | EQH-3 | | Recent | Early | Neandertals |
|--|------------|-------------|---|--------------------------|----------------------------------|
| | Left tibia | Right tibia | <i>H. sapiens</i> | <i>H. sapiens</i> | |
| Midshaft circumference (mm) | 103 | 96 | N/A | 84–96 ± 10 | 86 ± 8 |
| Robusticity index | 8.0 | 7.7 | 6.2–7.1 ± 0.5 [‡] (range of means of various human populations) | 6.7 ± 0.4 [‡] | 8.1 ± 0.5 [‡] |
| Distal tibia maximum ML breadth (mm) | N/A | 51.14 | N/A | N/A | 54 (Shanidar) |
| Distal tibia maximum AP length (mm) | N/A | 36.9 | N/A | N/A | 39.3 (Shanidar) |
| Distal articular facet maximum ML breadth (mm) | N/A | 29.53 | N/A | N/A | 31.3–32 (Shanidar) |

| Measurement | EQH-3 | | Recent | Early | Neandertals |
|---|------------|-------------|--|--|---|
| | Left tibia | Right tibia | <i>H. sapiens</i> | <i>H. sapiens</i> | |
| Distal articular facet, medial end, maximum AP length (mm) | N/A | 25.73 | N/A | N/A | N/A |
| Distal articular facet, lateral end, maximum AP length (mm) | N/A | 33.5 | N/A | N/A | 28.6–33.0 (Shanidar) |
| Medial malleolus length (mm) | N/A | 18.5 | N/A | N/A | N/A |
| Crural index: (tibial length/femoral length) × 100 | | 81.5 | 84–90 ± 4.3 ^{**} (range of means of various human populations) | 85.1 ± 2.8 ^{**} (<i>N</i> = 25) | 78.8 ± 1.7 ^{**} (<i>N</i> = 9) |

*McCown & Keith (21)

†Walker, et al. (80)

‡Lovejoy & Trinkaus (37)

§González-Reimers, et al. (102)

[¶]Stringer, et al. (38)

[#]Trinkaus (69)

^{||}Trinkaus (33)

^{**}Porter (103)

SI 4 Table 5. The femur and tibiae of Neandertal males and females compared to the EQH-3 femur and tibiae.

| Measurement | Male | Female | EQH-3 |
|---------------------------|------------------------|------------------------|---------|
| | $X \pm sd (N)$ | $X \pm sd (N)$ | |
| Femoral bicondylar length | $442.8 \pm 20.4 (9)^*$ | $400.3 \pm 14.3 (3)^*$ | 438 |
| Tibial length | $354.4 \pm 19.3 (8)^*$ | $310.0 \pm 9.5 (3)^*$ | 357 |
| Femur robusticity index | $7.19 \pm 0.59 (8)^*$ | $6.91 \pm 0.62 (3)^*$ | 7.4 |
| Tibial robusticity index | $8.24 \pm 0.4 (7)^*$ | $7.78 \pm 0.49 (3)^*$ | 7.7–8.0 |
| Tibial cnemic index | $68.9 \pm 6.6^\dagger$ | $74.8 \pm 0.5^\dagger$ | 61 |

^{*}Trinkaus (69)

[†]Trinkaus (33)

SI 4 Table 6. Estimated stature of EQH-3.

| Estimation Method | Reference | Population | Formula | Stature estimation for EQH-3 |
|--------------------|-----------------------|-------------------------|---------------------------|------------------------------|
| Femur length (FEL) | Sjøvold (104) | All races | $2.71 \times FEL + 45.86$ | $164.6 (\pm 4.49)$ |
| Femur length | Trotter & Gleser (89) | European-American males | $2.38 \times FEL + 61.41$ | $165.6 (\pm 3.27)$ |

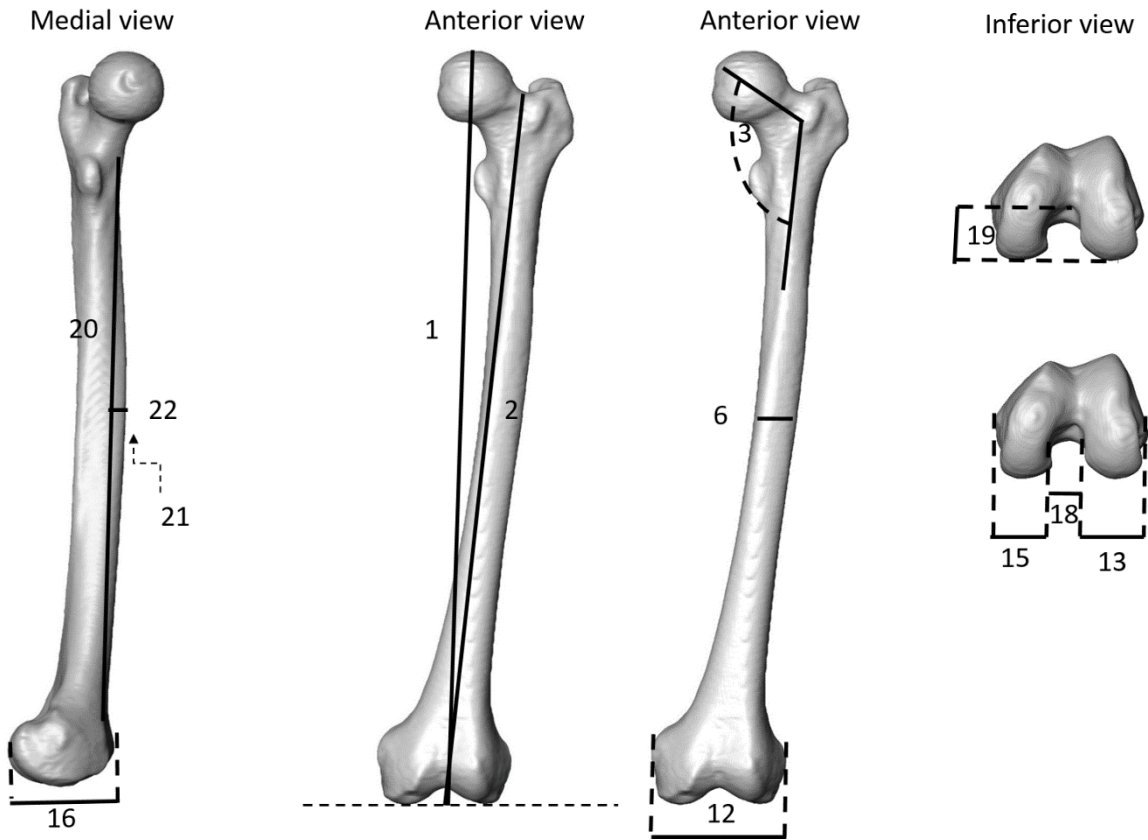
| Estimation Method | Reference | Population | Formula | Stature estimation for EQH-3 |
|-------------------------------|-----------------------|-----------------------------------|--|-------------------------------------|
| Femur length | Trotter & Gleser (89) | African-American males | $2.11 \times \text{FEL} + 70.35$ | 162.8 (± 3.94) |
| Tibia length (TL) | Sjøvold (104) | All races | $3.29 \times \text{TL} + 47.34$ | 165 (± 4.15) |
| Tibia length | Trotter & Gleser (89) | European-American males | $2.52 \times \text{TL} + 78.62$ | 168.6 (± 3.37) |
| Tibia length | Trotter & Gleser (89) | African-American males | $2.19 \times \text{TL} + 86.02$ | 164.2 (± 3.78) |
| Tibia length | Auerbach & Ruff (91) | North American Arctic males | $2.55 \times \text{TL} + 69.51$ | 160.5 (± 2.99) |
| (Femur and tibia) length | Trotter & Gleser (89) | European-American males | $1.39 \times (\text{FEL} + \text{TL}) + 53.2$ | 163.7 (± 3.55) |
| (Femur and tibia) length | Trotter & Gleser (89) | African-American males | $1.26 \times (\text{FEL} + \text{TL}) + 59.72$ | 159.9 (± 3.28) |
| Femur length and tibia length | Auerbach & Ruff (91) | North American Arctic males | $(1.28 \times \text{FEL}) + (1.26 \times \text{TL}) + 59.86$ | 160.9 (± 2.62) |
| Femur length and tibia length | Auerbach & Ruff (91) | North American Great Plains males | $(1.88 \times \text{FEL}) + (0.76 \times \text{TL}) + 54.13$ | 163.6 (± 1.94) |

| Estimation Method | Reference | Population | Formula | Stature estimation for EQH-3 |
|----------------------------------|-----------|------------|---------|------------------------------|
| Mean of stature values for EQH-3 | | | | 163.6 |

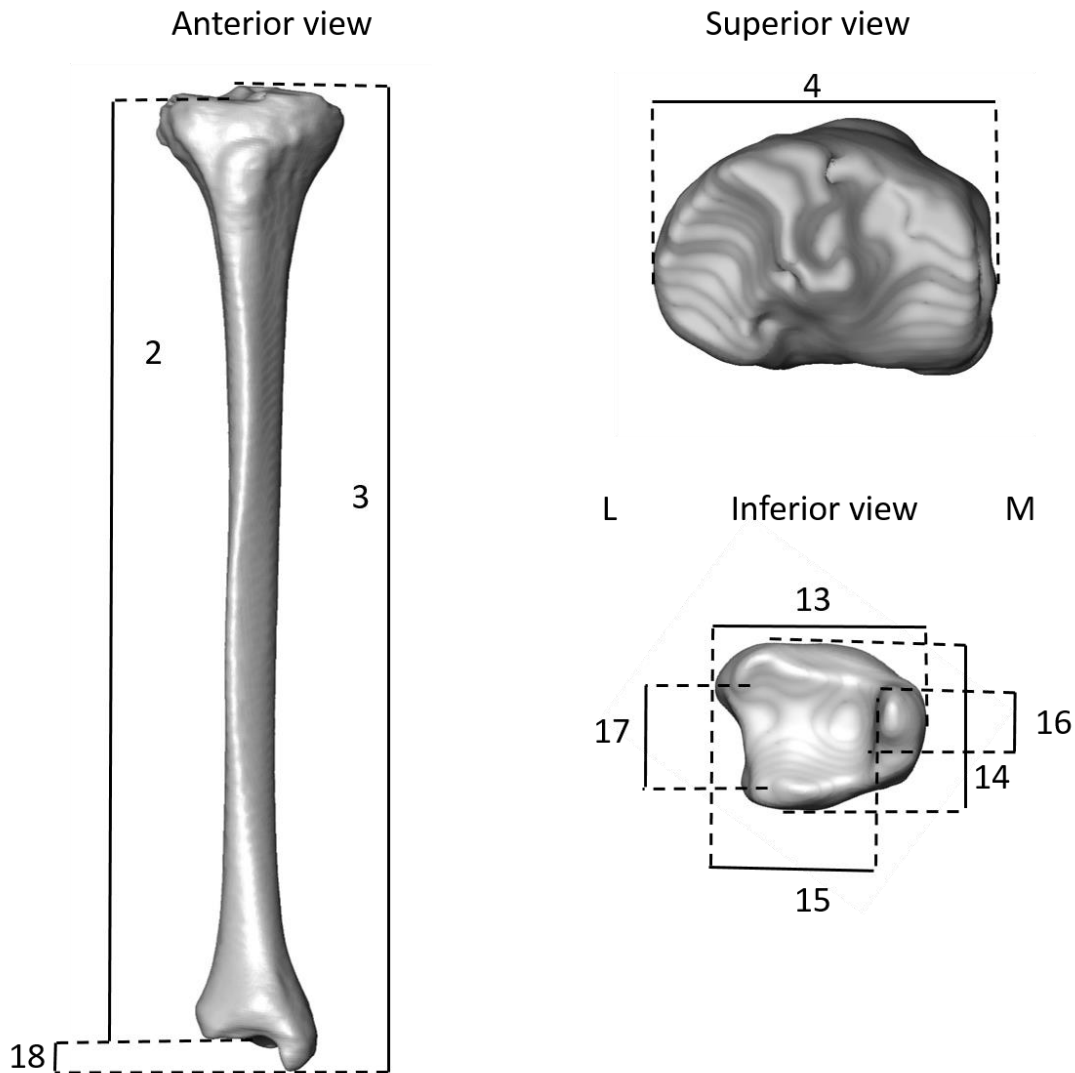
SI 4 Table 7. Comparison of stature estimation for EQH-3, recent *H. sapiens*, early *H. sapiens*, Neandertals, and Sima de los Huesos hominins.

| Population | EQH-3 | Recent <i>H. sapiens</i> * | Early <i>H. sapiens</i> * | Neandertals* | Sima de los Huesos hominins* |
|-----------------|-------|---|---------------------------|--------------|------------------------------|
| Males & females | 163.6 | N/A | 177.45 | 160.6 | 163.6 |
| Males | N/A | Range of means for 124 human populations: 144.1–184.9 | 185.1 ± 7.1 | 166.7 ± 5.9 | 169.5 ± 4.0 |
| Females | N/A | Range of means for 124 human populations: 137.0–167.7 | 169.8 ± 6.5 | 154.5 ± 4.6 | 157.7 ± 2.0 |

*Data from Carretero, et al. (40)



SI 4 Fig. 1. Femoral measurements. The numbers correspond to the measurement numbers in SI 4 Table 1.



SI 4 Fig. 2. Tibial measurements. The numbers correspond to the measurement numbers in SI 4

Table 2.

References

70. Nir, N. Bones and formation processes in the open-air Middle Paleolithic site of Ein Qashish. *MA thesis, Institute of Archaeology*. (The Hebrew University of Jerusalem, 2016).
71. Davidovich, U., Porat, N., Gadot, Y., Avni, Y., & Lipschits, O. Archaeological investigations and OSL dating of terraces at Ramat Rahel, Israel. *J. Field. Archaeol.* **37**, 192–208 (2012).
72. Murray, A.S., & Wintle, A.G. Luminescence dating of quartz using an improved single aliquot regenerative-dose protocol. *Radiat. Meas.* **32**, 57–73 (2000).
73. Galbraith, R.F., & Roberts, R.G. Statistical aspects of equivalent dose and error calculation and display in OSL dating: an overview and some recommendations. *Quat. Geochronol.* **11**, 1–27 (2012).

74. Nambi, K.S.V., & Aitken, M.J. Annual dose conversion factors for TL and ESR dating. *Archaeometry* **28**, 202–205 (1986).
75. Faershtein, G., Porat, N., Avni, Y., & Matmon, A. Aggradation-incision transition in arid environments at the end of the Pleistocene: an example from the Negev Highlands, southern Israel. *Geomorphology* **253**, 289–304 (2016).
76. Frayer, D.W. *Evolution of the Dentition in Upper Paleolithic and Mesolithic Europe*. University of Kansas Publications in Anthropology (vol. 10), (Lawrence, Kansas, 1978).
77. Suzuki, H., & Takai, F., Eds. *The Amud Man and His Cave site* (Academic Press of Japan, 1970).
78. Wolpoff, M.H. The Krapina dental remains. *Am. J. Phys. Anthropol.* **50**, 67–113 (1979).
79. Vandermeersch, B. *Les Hommes Fossiles de Qafzeh (Israël)* (Centre National de la Recherche Scientifique, Paris, 1981).
80. Walker, M.J., Ortega, J., Parmová, K., López, M.V., & Trinkaus, E. Morphology, body proportions, and postcranial hypertrophy of a female Neandertal from the Sima de las Palomas, southeastern Spain. *Proc. Natl. Acad. Sci.* **108**, 10087–10091 (2011).
81. Beauval, C., et al. A late Neandertal femur from les Rochers-de-Villeneuve, France. *Proc. Natl. Acad. Sci. USA* **102**, 7085–7090 (2005).
82. Stringer, C., & Gamble, C. *In Search of the Neanderthals: Solving the Puzzle of Human Origins* (Thames and Hudson, 1993).
83. Ruff, C.B. Climatic adaptation and hominid evolution: the thermoregulatory imperative. *Evol. Anthropol.* **2**, 53–60 (1993).
84. Weaver, T.D. The shape of the Neandertal femur is primarily the consequence of a hyperpolar body form. *Proc. Natl. Acad. Sci.* **100**, 6926–6929 (2003).
85. Trinkaus, E., & Ruff, C.B. Diaphyseal cross-sectional geometry of Near Eastern Middle Palaeolithic humans: The Tibia. *J. Archaeol. Sci.* **26**, 1289–1300 (1999).
86. Patte, E. *Les Néandertaliens*. (Paris, Masson et Cie, 1955).
87. Taylor, J.V. *The Neandertal Tibia*. PhD thesis. Columbia University (Ann Arbor, University Microfilms, 1968).
88. Trotter, M. Estimation of stature from intact long limb bones. *Personal Identification in Mass Disasters*. (ed. T.D. Stewart) 71–84 (Smithsonian Institution, National Museum of Natural History, Washington, DC, 1970).
89. Trotter, M., & Gleser, G.C. Estimation of stature from long bones of American Whites and Negroes. *Am. J. Phys. Anthropol.* **10**, 463–514 (1952).
90. Feldesman, M.R., & Lundy, J.K. Stature estimates for some African Plio-Pleistocene fossil hominids. *J. Hum. Evol.* **17**, 583–596 (1988).
91. Auerbach, B.M., & Ruff, C.B. Stature estimation formulae for indigenous North American populations. *Am. J. Phys. Anthropol.* **141**, 190–207 (2010).
92. Lieberman, D.E., Devlin, M.J., & Pearson, O.M. Articular area responses to mechanical loading: effects of exercise, age, and skeletal location. *Am. J. Phys. Anthropol.* **116**, 266–277 (2001).
93. Stäubli, H.U., & Rauschnig, W. Tibial attachment area of the anterior cruciate ligament in the extended knee position. *Knee Surg. Sport. Tr. A.* **2**, 138–146 (1994).
94. Perugia, D., Basiglioni, L., Vadala, A., & Ferretti, A. Clinical and radiological results of arthroscopically treated tibial spine fractures in childhood. *Int. Orthop.* **33**, 243–248 (2009).

95. Furlan, D., Pogorelić, Z., Biočić, M., Jurić, I., & Meštrović, J. Pediatric tibial eminence fractures: arthroscopic treatment using K-wire. *Scand. J. Surgery* **99**, 38–44 (2010).
96. Anderson, A.F., & Anderson, C.N. Correlation of meniscal and articular cartilage injuries in children and adolescents with timing of anterior cruciate ligament reconstruction. *Am. J. Sports Med.* **43**, 275–281 (2015).
97. Garralda, M.D., Galván, B., Hernández, C.M., Mallol, C., Gómez, J.A., & Maureille, B. Neanderthals from El Salt (Alcoy, Spain) in the context of the latest Middle Palaeolithic populations from the southeast of the Iberian Peninsula. *J. Hum. Evol.* **75**, 1–15 (2014).
98. Gaikwad, K.R., & Nikam, V.R. Sexual Dimorphism in Femur. *IOSR J. Dental. Medic. Sci.* **13**, 4–9 (2014).
99. Terzidis, I., et al. Gender and side-to-side differences of femoral condyles morphology: osteometric data from 360 Caucasian dried femora. *Anat. Res. Int.* doi:10.1155/2012/679658 (2012).
100. Ho, W.P., Cheng, C.K., & Liao, J.J. Morphometrical measurements of resected surface of femurs in Chinese knees: correlation to the sizing of current femoral implants. *The Knee* **13**, 12–14 (2006).
101. Nelson, D.A., Barondess, D.A., Hendrix, S.L., & Beck, T.J. Cross-Sectional Geometry, Bone Strength, and Bone Mass in the Proximal Femur in Black and White Postmenopausal Women. *J. Bone. Miner. Res.* **15**, 1992–1997 (2000).
102. González-Reimers, E., et al. Bending and torsional strengths of the tibia vs. simple anthropometric variables among the prehispanic population of El Hierro (Canary Islands). *Eur. J. Anat.* **18**, 8–15 (2014).
103. Porter, A.M.W. Modern human, early modern human and Neanderthal limb proportions. *Int. J. Osteoarchaeol.* **9**, 54–67 (1999).
104. Sjøvold, T. Estimation of stature from long bones utilizing the line of organic correlation. *Hum. Evol.* **5**, 431–447 (1990).